

1 **Preservation of Organic Carbon in Dolomitized Cambrian Stromatolites and Implications**
2 **for Microbial Biosignatures in Diagenetically Replaced Carbonate Rock**

3 ASHLEY E. MURPHY^{a*}, SCOTT T. WIEMAN^{b,c,d}, JULIANE GROSS^e, JENNIFER C. STERN^c, ANDREW
4 STEELE^f, MIHAELA GLAMOCLIA^a

5 *^aRutgers University, Department of Earth and Environmental Sciences, 101 Warren St, Smith*
6 *Hall – Room 135, Newark, NJ, 07102 (*corresponding author e-mail:*
7 *ashley.murphy@rutgers.edu)*

8 *^bCenter for Space Sciences and Technology, University of Maryland, Baltimore, MD 21250, USA*

9 *^cPlanetary Environments Laboratory, NASA Goddard Space Flight Center, Greenbelt, MD*
10 *20771, USA*

11 *^dCenter for Research and Exploration in Space Science and Technology, NASA Goddard Space*
12 *Flight Center, Greenbelt, MD 20771, USA*

13 *^dDepartment of Earth and Planetary Sciences, Rutgers University, New Brunswick, NJ 08854,*
14 *USA*

15 *^fGeophysical Laboratory, Carnegie Institution of Washington, Washington, DC, 20015, USA*
16

17 **ABSTRACT**

18 Stromatolites have been a major focus in the search for ancient microbial life, however, the
19 organic carbon biosignatures of dolomitized stromatolites have not yet been fully characterized
20 or correlated with their dolomitizing conditions. Although dolomitization rarely preserves
21 microbial morphology, the presence of organic carbon can provide valuable information for
22 characterization of fossils' biogenicity, syngenicity, and indigeneity to their host rock. The
23 Cambrian Allentown Formation in New Jersey, USA, is an excellent example of dolomitized
24 stromatolites and thrombolites containing diagenetically modified microbial biosignatures. Based
25 on XRD and EPMA data, the dolomite composition is typically stoichiometric, with varying
26 degrees of cationic ordering. The outcrop underwent early dolomitization in a marginal-marine
27 setting and later burial diagenesis resulting in multi-generational dolomite formation: (1)

28 microspar dolomite formed by early diagenetic replacement at or near the surface, (2) zoned
29 dolomite formed penecontemporaneously with the microspar phase as rhombohedral crystals by
30 infilling primary pore spaces within the microspar matrix. The rhombic crystals continued to
31 grow outward in alternating stages of Fe-enriched and -depleted fluids, which were preserved in
32 zoned rims and revealed by cathodoluminescence, and (3) saddle dolomite formed during late
33 stage deep burial with Fe- and Mn-rich fluids, and occurs as a void-filling, high-temperature
34 phase. Organic carbon, characterized using confocal Raman microscopy, has an exclusive
35 distribution within the microspar dolomite, and the D and G bands' characteristics reveal similar
36 thermal alteration to the host rock, indicating that the mapped organic carbon is indigenous and
37 syngenetic with the Cambrian carbonates. The findings presented in this study reveal organic
38 matter found within microspar of various dolomitized facies deriving from different source pools
39 of organic carbon. This study sheds light on biosignatures in secondary dolostones and may aid
40 biosignature detection in older carbonate rocks on Earth and Mars.

41

42 *Keywords:* dolomitization, Cambrian stromatolites, organic carbon, biosignatures, burial
43 diagenesis

44

45 **1. INTRODUCTION**

46 Stromatolites are microbially mediated sedimentary structures that record the oldest forms of
47 life on Earth (Barghoorn and Tyler, 1965; Grotzinger and Knoll, 1999; Allwood et al., 2006).
48 These ancient structures have drawn a significant focus of geobiology and astrobiology research
49 because of their ability to archive the interactions of biological, physical, and chemical processes
50 (e.g., Hoffman, 2013), providing an invaluable reference to Earth's past. A complication in the

51 reconstruction of these structures derives from the fact that, as any other rock and fossil,
52 stromatolites undergo diagenesis over time, which alters original biological signatures
53 (biosignatures), including chemical (e.g., organic carbon) and physical (e.g., cellular
54 morphology) evidence.

55 The most common diagenetic changes in stromatolites are silicification and dolomitization,
56 which involve the replacement of original calcium carbonate (CaCO_3) by silica (SiO_2) during
57 silicification and dolomite [$\text{CaMg}(\text{CO}_3)_2$] in dolomitization. Silicification during early diagenesis
58 leads to the exceptional preservation of original textures, microfossils, and organic chemistry,
59 which are leading indicators in the characterization of biogenicity, indigeneity (i.e., naturally
60 occurring in the environment), and syngenicity (i.e., formed at the same time as the enclosing
61 rock) (Knoll et al., 1988; Buick, 1990; Grotzinger and Knoll, 1999; Van Kranendonk et al.,
62 2003; Sugitani et al., 2007; Schopf and Kudryavtsev, 2012; Braiser et al., 2015). Unlike
63 silicification, dolomitization commonly results in the loss of microbial morphology (Schopf,
64 1999; Bartley et al., 2000), making the characterization of syngenetic and indigenous
65 biosignatures more difficult (Grotzinger and Rothman, 1996). Dolomite [$\text{CaMg}(\text{CO}_3)_2$] may
66 form during deposition (as primary dolomite) or post-deposition (secondary dolomite) from
67 various fluid chemistries and temperatures (Machel, 1978, 2004; Guido et al., 2018). The fate of
68 organic matter preserved under such a wide variety of conditions is yet to be properly evaluated.

69 Although the dolomitization process may be destructive to original stromatolitic textures and
70 compositions, studies of microfossils in dolomitic stromatolites have been reported. These
71 studies have interpreted the investigated dolomitic stromatolites as formed by primary dolomite
72 precipitation (Rao et al., 2003; Ayllón-Quevedo et al., 2007; Sanz-Montero et al., 2008; Calça et
73 al., 2016). The microfossils characterized in these primary dolomitic structures are preserved

74 exclusively in silica (Ayllón-Quevedo et al., 2007; Sanz-Montero et al., 2008; Calça et al., 2016)
75 and sulfur-rich mineral phases (Lindtke et al., 2011). In contrast, the effects of secondary
76 dolomitization on the preservation of organic material remain largely unexplored. Secondary
77 dolomitization may occur in a wide range of environments from the surface to deep burial
78 (several km depths) settings (Machel, 1978), under different temperatures and pressures, and as
79 such provides a range of settings that could be conducive to the long-term preservation of
80 organics. Characterizing the effects of secondary dolomitization on microbial fossil preservation
81 is critical for interpreting traces of early life in the geological record. The syngenicity and
82 indigeneity of this type of fossilization in the geologic record can only be comprehensively
83 examined after the degree of alteration of the host rock has been characterized and evaluated
84 against that of the biologic remains (Buick, 1990; Braiser et al., 2004).

85 The need for detailed insight into the preservation processes of organic matter, or
86 biosignatures in general, within dolomitized carbonate lithologies is also relevant to
87 astrobiology. Carbonate lithologies are a recognized astrobiology target for Mars exploration
88 (Cady et al., 2003; Summons et al., 2011; D'Elia et al., 2017). The primary science goal of the
89 Mars 2020 mission is to determine whether life existed on Mars by seeking signs of extinct life
90 in the rock record (Mustard et al., 2013; Williford et al., 2018). In February 2021, the Mars 2020
91 Perseverance rover will land in Jezero Crater, an ancient paleolake (~4.0-3.5 Ga) with a diverse
92 suite of carbonate-bearing terrains, including those with Mg/Ca compositions similar to
93 dolomites on Earth (Horgan et al., 2020). Although the origin of the magnesium carbonates
94 identified is still uncertain (Ehlmann et al., 2008; Goudge et al., 2015), the crater may contain
95 lacustrine carbonate deposits, which are habitable environments on Earth that provide the
96 potential for biosignature preservation (Horgan et al., 2020). Therefore, investigating organic

97 matter preservation in ancient dolomites on Earth can facilitate future searches for potential
98 biosignatures in Martian magnesium carbonates.

99 In this paper, we contrast the host rock alterations with the organic carbon contained within.
100 The measurements of whole rock and high-resolution *in situ* analysis of the three dolomite
101 mineral phases from the Cambrian Allentown Formation are used to characterize the
102 dolomitization setting. Confocal Raman spectroscopy is used to determine the spatial association
103 of organic carbon to minerals and their alteration. Finally, the results are used to evaluate the
104 level of diagenetic alteration that has affected the outcrop, and the effect that such alteration had
105 on the preservation of the organic carbon.

106

107 **2. GEOLOGIC SETTING**

108 **2.1. Regional geology and sedimentology**

109 The Late Cambrian (515-500 Ma) Allentown Formation (Weller, 1903; Howell, 1945; Harris
110 et al., 1995; Dalton et al., 2014), commonly referred to as Allentown Dolomite, is part of the
111 Kittatinny Supergroup (542-443 Ma). The Kittatinny Supergroup is a northeast trending
112 lithostratigraphic unit (Fig. 1) that records the formation of the eastern Laurentian (North
113 America) passive margin, when the deposition of shallow-water carbonates prevailed.
114 Paleoreconstruction of the area shows Laurentia positioned below the equator and rotated
115 approximately 90° clockwise from its current orientation (Blakey, 2016). During the Cambrian,
116 sediments from eroding inland rocks were transported by streams to the coast and deposited on
117 the shallow shelf (Miller, 1941; Dalton et al., 2014). The paleoenvironment has been interpreted
118 as shallow subtidal to supratidal resulting in the deposition of limestones that have been
119 subsequently dolomitized (Miller, 1941; Stead and Kodama, 1984; Dalton et al., 2014).

120 In the 1950s, the Allentown was divided into two members: the Limeport (bottom) and
121 Allentown Members (top) (Drake Jr., 1965). This distinction was made in older literature
122 because the lower Limeport Member contains numerous ‘cryptozoan’ features (hereafter referred
123 to as stromatolites) of various morphologies, including large domes with convex-shaped laminae,
124 wavy beds, and small domes of laterally linked laminae (Drake Jr., 1965). Previous geologic
125 mapping of the Allentown Formation reveals cyclic bedding (from oldest to youngest) as
126 follows: textureless dololutite (<0.0039 mm grain size), dolarenite (0.0625-2 mm), oolitic
127 dolarenite (0.0625-2 mm), dolorudite (>2 mm), cryptozoan (stromatolitic) dolomite, and
128 desiccation dolorudite (>2 mm) (Drake Jr., 1965). These inversely graded bedding cycles suggest
129 a regression sequence. Individual bedding cycles range in thickness from ~2 to 10 m, and the
130 entire formation sequence measures up to 580 m thick (Drake Jr., 1965; Monteverde, 1992).

131 **2.2. Study area**

132 The study area in Hamburg, New Jersey, USA, includes 40 m of uplifted dolostone
133 (dolomitic carbonate rock), tilted 44° NW. Exposure along the southwestern side of the outcrop
134 (Figs. 2, 3) allows for measurements of bedding thickness that are elsewhere inexact due to
135 glacially polished rock surfaces. Along the longest transect, the outcrop is 100 m long with
136 extensive vegetation cover that limits correlation between the northeast and southwest parts of
137 the outcrop (Fig. 3A). The southwest side of the outcrop does not contain microbial structures
138 (Fig. 3B), but the transect analyzed in the middle of the outcrop (Fig. 3A) contains stromatolites
139 and thrombolites. The bottom of transect A is ~13 m of fine-grained, grey dolosiltite intercalated
140 with iron oxidized dissolution seams that are weathered black in outcrop (Fig. 2B). The
141 occurrence of thrombolites (microbially mediated clotted structures) is marked by a brown wavy
142 layer of ~1 cm thick laminae (Fig. 2C). The thrombolites are overlain by small (≤ 5 cm). round

143 stromatolite heads (Fig. 2D, E) that occur periodically in overlying strata for ~20 m. Massive
144 oolitic dolarenite (Fig. 2F) is situated above the stromatolite heads for ~11 m. The oolitic
145 grainstone is overlain by ~13 m of dolosiltite with numerous beds of high energy, storm deposit
146 features of rip-up clasts (linearly stratified features) (Fig. 2G), edgewise conglomerates (Fig.
147 2H), and jumbled intraclasts (non-linearly stratified and randomly dispersed features) (Fig. 2I).
148 These beds co-occur with coarse-grained dolomite-filled vugs (≤ 9 mm) (Fig. 2J). Large (≤ 30 cm)
149 domal stromatolites, as well as intraclasts and collapse breccia are observed at the top of the
150 formation (Fig. 2K). The northeast side of the outcrop reveals the convex up structure of the
151 domes (Fig. 2L). Mudcracks (continuous polygonal morphology) are situated above the large
152 domal stromatolites (Fig. 2M) at the top of transect A, and syneresis cracks (discontinuous
153 sinuous morphology) are observed southwest of the stromatolites at the top of transect B (Fig.
154 2N). Transect B and sampling point marked by an asterisk (*) (Fig. 3) are dominated by oolitic
155 facies. Wavy stylolites parallel to bedding are found throughout the formation (Fig. 2O). Chert
156 occurs as black lenses or thin layers (~1 cm) throughout the formation (Fig. 2P). This bedding
157 sequence corresponds to a peritidal marine regression (Wilson, 1975; Flügel, 2004) (Fig. 1C).
158

159 **3. MATERIALS AND METHODS**

160 **3.1. Sampling strategy**

161 Samples ($n = 22$) were collected from 2017 to 2020 in Hamburg, New Jersey, USA. The
162 sampling strategy included twenty-two different sampling points, from bottom to top of the
163 formation, while targeting obvious stromatolitic morphologies and significant changes in strata
164 texture or appearance (Fig. 3). Sampled transects are marked A and B (Fig. 3) and the starting
165 letter of each sample name (Table 1) corresponds to the transect where the sample was collected,

166 samples labeled *12b-d are not part of either transect but rather the samples that exhibited
167 characteristic textures and were collected at sides of the transects. Table 1 lists samples from
168 bottommost (*12d) to the topmost bedding layers (A18) and what samples were included in
169 which analyses in this study. Hand-sized samples were collected in an organically clean manner
170 to avoid contamination by using gloves to handle samples that were wrapped in sterile aluminum
171 foil and placed in canvas bags. Subsampling was performed in the laboratory using a diamond
172 blade saw and deionized water to cut away outer rock layers from the interior areas that were
173 later used for analyses.

174 **3.2. Petrographic and mineralogical analyses**

175 Petrographic analyses of 14 texturally different layers were used to describe the stromatolites
176 and associated dolostones. The petrographic study involved plane polarized and cross polarized
177 light inspection of thin sections for textural and mineral identification, as well as to target regions
178 of interest for further spectroscopy. The detection of minor mineral phases was performed by
179 scanning electron microscopy with energy dispersive X-ray spectroscopy (SEM/EDS) at Rutgers
180 University using a Hitachi S-4800 operating at 15 to 20 kV and 12 to 15 uA, equipped with an
181 Apollo X EDAX.

182 Powder X-ray diffraction (XRD) of whole rock samples was used to determine dominant
183 mineral assemblages in 21 samples. The equipment used at Rutgers University was a Bruker D8
184 with a Cu-K α radiation. Operational settings were 40 kV, 25 mA. XRD spectra were collected
185 over the 2 Θ range of 5-75 $^{\circ}$ and with a step size of 0.02 $^{\circ}$ or 0.04 $^{\circ}$ and a count time of 48 or 115 s
186 per step, respectively. Identification of peak patterns was performed in DIFFRAC suite. Eva
187 V3.1 software using the International Center for Diffraction Data database (version PDF2013).
188 Backgrounds were subtracted before calculating d-spacing values. Stoichiometry was calculated

189 by taking the 2Θ value of the d_{104} peak, and converting the 2Θ to d-spacing using Bragg's Law
190 (Bragg and Bragg, 1913), and lastly, using the equation in Lumsden (1979) which relates the d-
191 spacing of the d_{104} peak to mol% of CaCO_3 . The equation derived by Lumsden (1979) can result
192 in ≤ 3 mol% CaCO_3 inaccuracies (Reeder and Sheppard, 1984), and therefore this stoichiometric
193 data was checked by electronprobe microanalysis data. The degree of cation ordering was
194 calculated by the intensity ratio of the d_{015} and d_{110} peak (Graf and Goldsmith, 1956; Goldsmith
195 and Graf, 1958). Reported values of dolomite stoichiometry and degree of cation order represent
196 bulk sample averages only (Table 2).

197 **3.3. Geochemical analyses**

198 $\delta^{13}\text{C}_{\text{dolo}}$ and $\delta^{18}\text{O}_{\text{dolo}}$ were analyzed via acidification of each powdered sample at 60°C using
199 85% H_3PO_4 . Analyses were carried out on a GasBench II System (Thermo) coupled to a Delta V
200 Plus isotope ratio mass spectrometer (IRMS) (Thermo) at NASA Goddard Space Flight Center.
201 Bulk (n=16) samples were chosen based on texture and mineralogy differences and were
202 analyzed to determine the isotope ratios of dolomite. Micro-drilled (n=7) samples were sampled
203 from thin-section billets at Rutgers University using a Medenbach micro-drill in order to isolate
204 microspar and saddle dolomite phases for comparison to the bulk rock, and to target the
205 minimum and maximum temperature of formation. The bulk samples were analyzed in triplicate,
206 and micro-drilled samples were analyzed in, at minimum, two replicates. Standards were run
207 before, in the middle of, and after each run. Precision is based on reproducibility of NIST
208 reference standard NBS-19 at $\pm 0.05\text{\textperthousand}$ for $\delta^{13}\text{C}_{\text{dolo}}$ and $\pm 0.15\text{\textperthousand}$ for $\delta^{18}\text{O}_{\text{dolo}}$. Isotopic values are
209 reported relative to the Vienna Pee Dee Belemnite (VPDB) (Table S1 in supplementary
210 material).

211 Organic carbon abundance, nitrogen abundance, and $\delta^{13}\text{C}_{\text{org}}$ were determined using an
212 Elemental Analyzer (Costech) coupled to a Delta V Plus IRMS (Thermo) at NASA Goddard
213 Space Flight Center. Powdered samples were placed in ashed (500°C) glass vials. Sedimentary
214 organic material was separated via dissolution in 6N HCl for approximately 48-96 hours.
215 Insoluble material was allowed to settle before samples were carefully decanted and then left to
216 dry. The complete dissolution of carbonates was verified using SEM/EDS microscopy. Dry
217 insoluble material was scraped out of glass containers, weighed, and packed into tin capsules for
218 analyses. Standards were analyzed periodically during each run to assess the precision of the
219 measurements. Precision is based on reproducibility of reference standard USGS40 (glutamic
220 acid) at $\pm 0.07\%$ for $\delta^{13}\text{C}_{\text{org}}$. Isotope values are reported relative to VPDB standard and total
221 organic carbon as wt% (Table S1 in supplementary material). To calculate wt% organic carbon,
222 the analyzed sample's weight was divided by its total weight (pre-dissolution) and multiplied by
223 100%. The residual % of organic carbon measured was then converted to total organic carbon
224 (TOC) by the following equation:

$$225 \quad \text{TOC} = ((\text{organic carbon measured}) * (\text{analyzed sample weight} / \text{initial sample weight})).$$

226 Qualitative elemental X-ray mapping (n=2) and cathodoluminescence (CL) mapping (n=9)
227 was performed on thin sectioned samples with the JEOL Superprobe JXA-8200 at Rutgers
228 University. Samples were chosen based on texturally different microscale features. Operating
229 conditions were 15 kV accelerating voltage, 14 nA beam, focused beam diameter (~ 1 micron), a
230 step size of 1 μm , and a dwell time of 30 ms. The $\text{K}\alpha$ X-ray maps and CL maps were processed
231 with the xCLent software at Rutgers University to create red, green, and blue (RGB) colored
232 composite maps of the sample.

233 Quantitative electronprobe microanalyses (EPMA) of mineral composition were obtained on
234 7 samples with the JEOL Superprobe JXA-8200 at Rutgers University, to isolate each phase of
235 dolomite. Operating conditions were 15 kV accelerating voltage, 15 nA beam current, and a
236 beam diameter of 5 microns. Analytical standards were well-characterized synthetic oxides and
237 minerals including strontianite (Sr), orthoclase (Si), fayalite (Fe), rhodonite (Mn), calcite (Ca),
238 ZnO (Zn), and dolomite (Mg). Data quality was ensured by analyzing secondary standard
239 materials as unknowns. Average detection limits (in oxide wt%) are SrO = 0.03; MnO, SiO₂,
240 FeO = 0.02; CaO, MgO = 0.01; and ZnO = 0.17. The average analytical errors for elements
241 above detection limit are: Ca ~0.25%; Mg ~0.47%; Fe ~5.36%; and Mn ~46%. Stoichiometry
242 (Mg/Ca) was calculated for each phase of dolomite. Stoichiometry was determined by converting
243 the average elemental wt% of Mg and Ca for each dolomite phase to mol% Mg and Ca, where
244 total percentage of Mg and Ca was normalized to 100. Results are reported in Table 2 and Table
245 S2 in supplementary material.

246 **3.4. Confocal Raman microscopy**

247 Confocal Raman microscopy and spectroscopy was used for spot analyses and mapping of 14
248 thin sections and 8 unprocessed rock samples, to determine the organic carbon spatial
249 distribution, associations with minerals, and to analyze the D and G bands (~1350 and 1600 cm⁻¹,
250 respectively) characteristic Raman signal for the organic matter. Five thin sections were chosen
251 for the final high-resolution analysis. These representative layers ranged across the top, middle,
252 and bottom areas of the outcrop and include all lithological textures observed (Fig. 3, Table 1).
253 This work was performed at Rutgers University with a WITec alpha300 equipped with a
254 frequency-doubled Nd:YAG (532 nm) excitation laser. Operational settings were as follows: a 1
255 mV average laser intensity (range from 1-3 mV) to minimize laser-induced heating and to avoid

256 structural modification of the samples, and a depth of 1-5 μm below the surface was used to
257 avoid surface contamination. Mapped areas were visually inspected by transmitted and reflected
258 light microscopy for holes and cracks in the samples that may contain polishing grit, epoxy, or
259 other contaminants related to sample handling that may interfere with the D and G band spectra.
260 Samples that could not be unambiguously identified as unaffected by this type of contamination
261 or were too friable for thin sectioning were not included in the final Raman data sets.

262 D and G bands were analyzed in two ways for data quality assessment, using (1) WITec
263 Project FIVE+ software cluster analysis, and (2) WITec Project FIVE+ software Gaussian fitted
264 background subtraction. The cluster method identifies variations in D and G band phases within
265 a map, averages it, and displays a distribution map. Ten clusters of spectral variations were
266 calculated from each map, and one to three were chosen from each mapped area after quality
267 evaluations (signal-to-noise ratio, surface contamination, and interference bands from hematite
268 were avoided after being inspected both visually and spectrally). The Gaussian fit method uses a
269 Savitzky-Golay filter to smooth the graph before applying background subtraction using a
270 Gaussian fit for both the G and D bands. The average D and G band peak centers are displayed
271 on a distribution map where one to three spectral points, representative of different spectral
272 trends, were hand selected. Maps were inspected for visual and spectral interferences as listed
273 above in the cluster analysis method.

274 The D and G band cluster results were deconvoluted into five peaks (D1, D2, D3, D4, and G)
275 using PeakFit 4.12 software and following the methodology for peak fittings F and E in
276 Kouketsu et. al. (2014). The numeric table exported from the PeakFit software was used to report
277 all peak parameters including the full width at half maximum (FWHM) used to determine
278 temperature of alteration (Table 4, and Tables S3c, S3d in supplementary material). Organic

279 carbon first-order bands of Raman spectra (D and G bands at ~1350 and 1600 cm⁻¹, respectively)
280 record the host rock's maximum temperature and can be used as an organic paleothermometer
281 (Pasteris and Wopenka, 1991; Wopenka and Pasteris, 1993; Marshall et al., 2001, 2012). The G
282 band represents the ordered, graphitic structure of carbon, and the D band represents the
283 disordered carbon structure. Variations in the bands, related to differing amounts of thermally
284 induced rearrangement, can be used to determine structural order of the carbon and associated
285 temperature setting required for such level of crystallinity (Pasteris and Wopenka, 1991; Beyssac
286 et al., 2002). Thermometry was calculated using the D1 band geothermometer from Kouketsu et
287 al. (2014):

$$288 \quad T(\text{°C}) = -2.15 * (\text{FWHM-D1}) + 478 (\pm 30\text{°C})$$

289 This widely used geothermometer was chosen due to the consistency of FWHM with
290 temperature (Kouketsu et al., 2014). A two-tailed, two-sample *T*-test (*p*=0.05) was applied to D1
291 and D2 spectral data to determine if variations within the bands and derived temperatures were
292 statistically different (Figs. S1, S2 in supplementary material).

293

294 **4. RESULTS**

295 **4.1. Allentown petrology and mineralogy**

296 *4.1.1. Bulk mineralogy*

297 Based on powder X-ray diffraction (XRD) (Fig. S3 in supplementary material) the
298 mineralogy of the Allentown Formation is predominantly dolomitic with few 1-40 cm thick,
299 greyish-black chert lenses (Fig. 2P), and ~1 cm brown colored feldspathic carbonate layers (Fig.
300 2C) (samples A15, B15b, and A6, respectively). The feldspathic (orthoclase and microcline)
301 carbonate layers occur as thin wavy layers or disk-shaped forms and are commonly observed

302 along fractured bedding surfaces or at the top of microbial macrostructures. Results for
303 stoichiometry and cation ordering are presented in Table 2. The average d-spacing of the
304 dolomite d_{104} peak is 2.889 Å and ranges 2.854 – 2.894 Å ($1\sigma = 0.009$) for (n=20) samples.
305 These d-spacings indicate that the stromatolite (A16) and thrombolite (A5) are stoichiometric
306 (50.0 and 49.7 mol% CaCO_3 , respectively). The sample B11 has low Mg-excess (49.3 mol%
307 CaCO_3), and the cherty outlier (B15b) is 39.3 mol% CaCO_3 , and the remaining samples range
308 from 51-53 mol% CaCO_3 (Table 2). The 14 samples show low Ca-excess of <53 mol% CaCO_3 ,
309 and 2 samples are 52.7 mol% CaCO_3 . Reported values are derived from bulk rock measurements
310 and therefore represent sample averages, which may include an error of up to 3 mol% CaCO_3
311 due to the Lumsden (1979) calculation used (Reeder and Sheppard, 1984). The average degree of
312 cation order calculated by the d_{015}/d_{110} intensity ratio is 0.67 and ranges 0.36 – 0.99 ($1\sigma = 0.16$)
313 for (n=18) samples (Table 2). The range of cationic ordering ratios represent poorly- to well-
314 ordered dolomite, respectively (Kaczmarek and Sibley, 2011; Pina et al., 2020). Most samples
315 (n=13) are ≥ 0.60 which is indicative of relatively well ordered dolomite (Kaczmarek and Sibley,
316 2011). Cherty and feldspathic carbonate samples did not exhibit d-peaks of (015) or (110) in
317 XRD, and therefore these samples were not included in the stoichiometry and cation ordering
318 averages. Since these analyses are bulk sample measurements, the reported values represent
319 sample averages and are not characteristic of the individual dolomite phases. Stoichiometry for
320 individual dolomite phases was conducted using EPMA spot analyses.

321 **4.2. Microscale textures and mineralogy**

322 *4.2.1. Multi-phase dolomite characterization*

323 Composite Red-Green-Blue (RGB) cathodoluminescence maps with Red = 450-500 nm,
324 Green = 400-450 nm, and Blue = 350-400 nm reveal three distinct phases of dolomite in all

325 analyzed samples (Figs. 4, 5). Dolomite phases vary in crystal size, shape, and intercrystalline
326 boundaries. The three phases of dolomite are classified and characterized by increasing grain
327 size, as microspar, zoned, and saddle, respectively (Fig. 4). The microspar (M) dolomite is
328 nonplanar, and has closely packed anhedral crystals with irregular, intercrystalline grain
329 boundaries (Fig. S4 in supplementary material). The crystals average 20 microns and range 5-40
330 microns in size. Zoned (Z) dolomite is planar, subhedral to anhedral medium grained (10-100
331 microns) with straight compromised boundaries (Fig. 5B). The crystals are concentrically zoned
332 in CL, but not in plane polarized light, and are characteristically pore lining or void-filling (Figs.
333 4E, 5). Saddle (S) dolomite is nonplanar, medium (10-100 microns) to coarse grained (>100
334 microns) saddle-shaped, void-filling, and exhibits undulatory extinction in cross polarized light
335 (Fig. 6D, E). The three observed CL colors, by increasing wavelength, are blue, grey, and gold,
336 and are found throughout the microspar and zoned dolomite phases; the saddle dolomite only
337 exhibits a dull bluish color in CL (Fig. 4E). Throughout each phase of dolomite, two CL spectral
338 peaks are present at 389 nm and 650 nm (Fig. 4D).

339 *4.2.2. Porosity types and dissolution features*

340 Open porosity is absent in the studied samples, but occluded pore types of primary and
341 secondary origins were observed. Primary fenestral porosity (≤ 1 mm in size) is ubiquitous in
342 stromatolite samples and infilled with zoned and saddle dolomite (Fig. 7A-C). Vugs are large (2
343 - 9 mm in average) secondary pores that are at least two times greater in size than the microspar
344 matrix, and are infilled with zoned and saddle dolomite (Fig. 2J). Vugs occur predominately in
345 layers with rip-up clasts and are absent from the lowermost finer grained facies. Secondary
346 microfractures occur in two stages. The first stage includes vertical microfractures (< 1 mm
347 wide), infilled with zoned and saddle dolomite, that are present in limited layers of microspar

348 dolomite, and crosscut horizontal laminae and fenestrae in the domal stromatolite (Fig. 7E). The
349 second stage includes randomly oriented microfractures (<1 mm wide) that are present in the
350 oolitic dolosiltite sample B14 and are only infilled with saddle dolomite (Fig. S5 in
351 supplementary material).

352 Dissolution structures of numerous solution seams occur on fresh surfaces as brownish,
353 irregular streaks but appear black on weathered surfaces, and are abundant in the lowermost
354 outcrop layers of finely crystalline, microspar dolomite samples (Fig. 6F). The seams are Fe
355 oxidized-stained but composed of dolomitic material. Microstylolites that parallel the laminae
356 occur throughout sample A3 (Fig. 6G). Stylolites are either dolomitic in composition or, when
357 found along fractured bedding planes, are infilled with quartz, feldspars, and iron oxides.

358 *4.2.3. Thrombolites*

359 The thrombolites exhibit clotted, irregular microtextures (Fig. 6B, C). Rounded microcline
360 and orthoclase, and sub-rounded quartz occur throughout the sample, with small amounts of
361 peloids and ghost grains. SEM/EDS reveals minor mineral components of Fe-oxides and pyrite
362 grains. The detected metal oxide morphologies range from euhedral to highly deformed in shape,
363 and the pyrite has round to sub-round edges (Fig. S6 in supplementary material).

364 *4.2.4. Ooids*

365 The oolitic dolomite layers exhibit nonmimetic replacement (Sibley, 1978) where little or no
366 original texture (radial or tangential) visible except for a dark-colored ooid outline and relics of
367 concentric layers near the nucleus of the ooid (Fig. 8). Ooids vary in size from ~0.25 to 1 mm in
368 diameter.

369 *4.2.5. Stromatolites*

370 The microtexture of the domal stromatolites consists of three distinctly colored layers, as
371 follows: dark grey thinly layered convex-shaped laminae (<1 mm thick), light grey thinly layered
372 convex-shaped laminae (\leq 1 cm thick) (Fig. 7F, G), and black, very thin (<1 mm) laminae (Fig.
373 7G). The dark and light grey layers alternate throughout the stromatolites, and the black layers
374 occur predominately in the lower half (Fig. 7G) of the large domal stromatolites. EDS showed no
375 differences in composition between dark and light grey bands of laminae. However, the black
376 laminae are enriched in felsic material (Fig. S7 in supplementary material). Primary fenestral
377 porosity (\leq 1 mm thick) in the domal stromatolite is parallel to laminae and infilled with zoned
378 and saddle dolomite (Fig. 7A, E). Very fine-grained, rounded intraclast rip-ups are situated on
379 the topmost layer (Fig. 7H), which also contains large (<0.5 mm in diameter), rounded feldspars
380 of microcline and orthoclase, and sub-rounded quartz grains. The orthoclase minerals exhibit
381 overgrowth rims (Fig. 7I). The SEM/EDS reveals Ti-oxides, Fe-oxides, pyrite and apatite as
382 minor mineral components (Fig. S6 in supplementary data).

383 **4.3. Geochemistry**

384 *4.3.1. Multi-phase dolomite high-resolution elemental analysis*

385 Each phase of dolomite was targeted for microanalyses by electron probe after identification
386 with CL. All three phases of dolomite contain Zn and Mn, and the microspar and zoned dolomite
387 phases have Si (Fig. 4F). The zoned dolomite exhibits dark banding associated with Fe
388 concentrations of 0.4 wt% or higher (Fig. 4G). A compositional trend is observed in the
389 microspar and zoned dolomite phases by a covarying increase in Si with a decrease in Ca and
390 Mg. A decrease in Si abundance and an increase in Fe and Mn abundance is observed across the
391 phases of dolomite (Fig. 4F). No Sr is detected in any phase. The average mol% Ca is 49.3%
392 (n=116 spots analyzed), 49.2% (n=130 spots analyzed), 50.8% (n=131 spots analyzed) for

393 microspar, zoned, and saddle dolomite, respectively (Table S2 in supplementary material). These
394 low Mg- and Ca-excess values translate to Mg/Ca ratio averages of 1.03, 1.03, and 0.97 for
395 microspar, zoned, and saddle dolomite phases, respectively (Table S2 in supplementary
396 material). These values represent stoichiometric microspar and zoned dolomite, and Ca-excess
397 saddle dolomite. The EPMA error for Ca is 0.25% and Mg is 0.47%, so reported values may be
398 closer to stoichiometric than shown.

399 *4.3.2. Carbonate $\delta^{18}\text{O}$ and $\delta^{13}\text{C}$ composition*

400 Isotope analysis reveals relatively low values of $\delta^{18}\text{O}_{\text{dolo}}$ (‰ VPDB) and $\delta^{13}\text{C}_{\text{dolo}}$ (‰ VPDB).
401 Oxygen isotopes ($\delta^{18}\text{O}_{\text{dolo}}$) range from -18.23‰ to -6.05‰ referenced to VPDB ($1\sigma = 2.79\text{‰}$)
402 (Fig. 9, Table S1 in supplementary material). Inorganic carbon isotopes ($\delta^{13}\text{C}_{\text{dolo}}$) range from -
403 6.54‰ to -0.84‰ referenced to VPDB ($1\sigma = 1.39\text{‰}$).

404 *4.3.3. Total organic carbon and organic $\delta^{13}\text{C}$ composition*

405 Elemental analysis shows that nitrogen abundance is below detection limits, and organic
406 carbon abundance ranges from 0.025 to 0.484 wt% ($1\sigma = 0.142 \text{ wt\%}$) (Fig. 10, Table S1 in
407 supplementary material). Values of $\delta^{13}\text{C}_{\text{org}}$ for organic compounds range from -28.25‰ to -
408 25.73‰ referenced to VPDB ($1\sigma = 0.81\text{‰}$).

409 **4.4. Confocal Raman microscopy**

410 Raman mapping of thin sections reveals that organic carbon, identified by D and G spectral
411 bands, is exclusively associated with the microspar dolomite and commonly situated at or near
412 grain boundaries (Fig. 11). The D and G peaks show slight variations among peak intensity, peak
413 area, and peak position (Fig. 12, Tables S3a and S3b in supplementary material). D and G peak
414 shifts within spectral maps are observed in samples A5 and A16, respectively (Fig. 11C, Figs.
415 S8a, S8b in supplementary material). *T*-test results reveal a statistical difference ($p < 0.05$) in D1

416 band positions between stromatolite and thrombolite samples compared to oolitic samples (Fig.
417 S1b in supplementary material). The peak shifts in the thrombolite (in D band) and stromatolite
418 (in G band) samples A5 and A16, spatially overlap and occur within the same mapped areas
419 (Figs. S8aC-E in supplementary material), suggesting there are co-occurrences of different
420 degrees of the organic matter crystallinity within the same analyzed area.

421 Data quality assessment was done by comparing the computer-fitted cluster method to the
422 more commonly used manually-fitted Gaussian method. Comparison shows that the results from
423 the two methods are in overall good agreement, but the Gaussian fit method causes a broader
424 range and relative standard deviation (Table 3). Cluster analysis shows D/G peak intensity ratios
425 average 1.00 ± 0.05 ; D-FWHM averages 68 ± 34 ; and D-position averages 1334 ± 12 . Gaussian
426 fit analysis shows D/G peak intensity ratios average 1.02 ± 0.75 ; D-FWHM averages 47 ± 57 ;
427 and D-position averages 1335 ± 26 . All peak parameter results from the cluster and Gaussian fit
428 methods are presented in the supplementary material (Tables S3a, S3b).

429 Temperatures derived from Raman geothermometry average $293 \pm 61^\circ\text{C}$, and D1 band
430 variations show distinct grouping within samples in both peak position (rel cm^{-1}) and FWHM
431 (Fig. 12). The sample grouping corresponds to different temperature ranges: temperature average
432 of $314 \pm 25^\circ\text{C}$ for oolitic samples; temperature average of $313 \pm 18^\circ\text{C}$ for stromatolite samples;
433 and temperature average of $271 \pm 27^\circ\text{C}$ for thrombolite samples (Table 4). *T*-test results for
434 fitting E method reveal a statistical difference ($p < 0.05$) among the temperature groups of
435 stromatolite (A16), oolitic (A7, B11, B12a) and thrombolite (A5) samples, while fitting F
436 method shows no statistical difference between facies (Figs. S2a, S2b in supplementary
437 material).

438

439 **5. DISCUSSION**

440 Characterization of the dolomitization process (including fluid composition and temperature)
441 is fundamentally important when attempting to decipher the origins and alteration levels of
442 organic matter within the host rock. The following sections characterize the depositional
443 environment and conditions for subsequent dolomitization based on outcrop observations
444 (structural and textural features), petrological (microtextural and cross-cutting relationships),
445 geochemical data, and Raman spectroscopy.

446 **5.1. Sedimentary facies and paleoenvironment**

447 Exposed stratigraphy displays a regression sequence where subtidal high energy ooid shoals
448 transition to intertidal low energy silty lagoonal waters that progress to a supratidal mudcracked
449 tidal flat (Fig. 1C). The dolomitized oolitic grainstone beds were likely ooid shoals that inhibited
450 the incursion of marine waters and formed lower energy lagoons in which overlying finer, silt-
451 sized deposits were formed. On top of the lagoonal deposits are finely laminated domal
452 stromatolites in the beds which also include mudcracks, collapse breccias, and tidal channel
453 deposits, indicative of nearshore, subaerial exposure (Fig. 2). The presence of edgewise
454 conglomerate rip-up clasts, jumbled intraclasts, and torn laminae in small stromatolite domes
455 (Fig. 2E) suggest occurrences of high energy storms in nearshore and shallow water. Some layers
456 of lagoonal dolosiltite contain sparse ooids, referred to as oolitic dolosiltite (Table 2). At the top
457 of the outcrop, on the southwest side and adjacent to the large domal stromatolites, are extensive
458 syneresis cracks (Fig. 2N). Syneresis cracks form subaqueously (Plummer and Gostin, 1981),
459 indicating that water levels may have been deeper within the same stratigraphic layer (southwest
460 from the stromatolites). The Allentown Formation's sedimentological features are consistent

461 with a shallowing peritidal lithological sequence from a transitional marginal-marine setting
462 (Wilson, 1975; Flügel, 2004).

463 *5.1.1. Microtexture and mineralogy*

464 The dark-to-light grey and black stromatolite laminae are characteristic features formed as a
465 result of different mineral assemblages. The data indicate that the black laminae are enriched in
466 silicate minerals, such as detrital quartz and feldspars (Fig. S7 in supplementary material). The
467 black laminae (<1 mm thick) may have formed during the periods of minor marine flooding
468 when only the smallest particles were carried by low energy waters across the microbial mats
469 (Wilson, 1975). Additionally, scattered siliceous fine grains are found along some dark and light
470 grey stromatolitic laminae, a feature characteristic in regression carbonate evaporitic cycles
471 (Wilson, 1975). Previous Allentown studies (Buie, 1932; Miller, 1941) have attributed the dark-
472 to-light grey color variation to laminae with different concentrations of organic matter and
473 magnesium, stating that beds with high magnesium weather to a lighter color, while beds with
474 lower magnesium and more organic content undergo less change in color during weathering. We
475 have not found any evidence of differences in magnesium content within dark-to-light grey
476 layers, and Raman mapping of organics does not show an increased concentration of organic
477 carbon content among dark grey and black laminae compared to light grey laminae.

478 Accessory minerals such as pyrite, quartz, and feldspars are most abundant in chert lenses
479 and feldspathic layers. Rounded pyrite and feldspar grains observed in petrological and SEM
480 micrographs indicate their detrital origin (Figs. 7H, S6C in supplementary material). The detritus
481 materials are likely fluvial (Dalton et al., 2014) and aeolian (Miller, 1941) sediments transported
482 by streams and wind, respectively. Ti-oxide phases include anatase and rutile, the former being
483 the most abundant, and these minerals are scattered throughout the samples and are not limited to

484 any specific layer(s). Fe-oxides are less common than Ti-oxides and occur sporadically
485 throughout the samples. The deformed (warped) Fe- and Ti-oxides observed in this study (Fig.
486 S6A in supplementary material) were likely altered in their original environment before final
487 deposition and therefore are not indicative of the deposition settings of the study area. Fine-
488 grained dolomite crystals, finely layered stromatolitic laminae, channel deposits with rip-up
489 clasts, and detrital feldspars and quartz are microtextures frequently observed in tidal flat
490 environments (Siedlecka, 1978; MacNaughton et al., 2019).

491

492 **5.2. Dolomitization**

493 Traces of precursory limestone of the Allentown Formation have not been identified (Dalton
494 et al., 2014), so the baseline for comparison of dolomitized geochemistry and setting to that of
495 the Cambrian marine setting is missing, which makes interpretations of diagenetic stages or
496 recrystallization settings more difficult. There is no evidence for non-stoichiometric metastable
497 magnesium carbonate minerals that are presumed to form during initial dolomitization stages,
498 indicating that the formation has been entirely replaced by dolomite.

499 Petrographic features, luminescence, and microprobe analyses suggest multistage
500 dolomitization. Dolomite petrography shows three texturally different crystal phases that are
501 compositionally different to one another (Fig. 4). Determining the order of dolomite crystal
502 formation is essential to reconstruct the paragenetic sequence (Fig. 13) and to reveal if chemical,
503 thermal, or textural overprinting by later crystal generations exists. The following sections
504 discuss the interpreted formation of each phase of dolomite.

505 *5.2.1. Dolomitizing Fluids*

506 The composition of dolomitizing fluids can be constrained by the relative abundance of
507 major and trace elements in dolomite, including the Mg/Ca ratio, Fe, Mn, Zn, Sr, and Si
508 concentrations (Morrow, 1982; Tucker and Wright, 1990; Gasparini et al., 2006; Zhang et al.,
509 2009; Guido et al., 2018). The Si concentrations detected within the dolomite are not well
510 understood and are rarely reported in literature. Silica was not detected in these areas using
511 Raman spectroscopy, suggesting that Si is not sourced from submicron fluid inclusions or
512 mineral coatings. Si detected by EPMA could have originated from dissolved silica in the
513 seawater during the dolomite's formation (Ramseyer et al., 2013; Dong et al., 2015). The lack of
514 detectable Sr in any of the dolomite phases may be the result of dolomitization in seawater with
515 low Sr content (Vahrenkamp and Swart, 1990), or recrystallization (Land, 1980). Cambrian
516 dolomites formed from seawater can have Sr compositions of <300 ppm (Vahrenkamp and
517 Swart, 1990; Jiang et al., 2019), which is below EPMA detection limits at 0.03 wt%. Therefore,
518 undetectable Sr (<300 ppm) is in line with that expected of dolomites formed from fluids with
519 typical seawater Sr/Ca ratios (Vahrenkamp and Swart, 1990). This, along with the detection of
520 Si, suggests that the Allentown microspar and zoned dolomite phases may have precipitated from
521 seawater (Fig. 4F). Alternatively, it is common in burial diagenesis that Sr and Na concentrations
522 decrease while Fe and Mn increase (Wright and Tucker, 1990; Warren, 2000). However, this
523 continuous increase in Fe and Mn observed across all dolomite phases when coupled with the
524 presence of saddle dolomite and stylolites indicate an increasing burial origin. The saddle
525 dolomite phase that is enriched in Mn and Fe was likely produced from burial fluids when
526 externally sourced fluids rich in Fe and Mn mixed with dolomitizing fluids that circulated
527 through the host rock in a water-buffered system (Budd, 1997).

528 *5.2.1.1. Microspar dolomite*

529 Microspar dolomite (M) is a finely crystalline replacive dolomite with microspar-sized
530 crystals (Folk, 1959). An average crystal size of 20 μm was estimated using confocal Raman
531 microscopy. Microcrystalline textures in dolomite (<10 microns) are thought to be from fluids
532 that are highly saturated with respect to dolomite (Sibley, 1991) and are common in early near-
533 surface dolomitization (Moore, 1989; Sibley, 1991; Lukoczki et al., 2020; Ryan et al., 2020).
534 This phase of dolomite exhibits nonplanar, irregular intercrystalline grain boundaries (Fig. S4 in
535 supplementary material), which is common for crystal growth at temperatures greater than 50°C
536 (Gregg and Sibley, 1984; Sibley and Gregg, 1987; Warren, 2000), however, this texture has also
537 been observed in microspar formed in low temperature, subaerial environments in the presence
538 of concentrated Mg ion solutions which enable rapid nucleation of crystals during dolomitization
539 (Sibley and Gregg, 1987; Sijing et al., 2014). In either case, the limestone dolomitized early in
540 the marginal marine setting that produced microspar dolomite, which is the dominant dolomite
541 phase in the studied outcrop (Fig. S4 in supplementary material). The preservation of primary
542 porosity (fenestral pores) and fine-scale stromatolitic laminae within microspar beds is evidence
543 for early, near-surface dolomitization (Fig. 7). Therefore, the microspar dolomite is likely a
544 result of rapid crystal growth under high fluid Mg/Ca ratios.

545 The CL spectral peaks at 389 nm and 650 nm (Fig. 4D) are due to intrinsic lattice defects in
546 the CO_3^{2-} structure and the substitution of Mg^{2+} with Mn^{2+} into the carbonate lattice, respectively
547 (Walker et al., 1989; Machel et al., 1991; Habermann et al., 1997; Richter et al., 2003).

548 Accordingly, the peak shift that is present at 389 nm (Fig. 4D) may be due to different types of
549 crystallographic lattice defects, and if so, variations in crystallographic defects may account for
550 the variations in CL colors of increasing wavelength from blue and grey, to gold (Fig. 4E).

551 *5.2.1.2. Zoned dolomite*

552 Zoned dolomite (Z) occurs as small rhombohedral shaped crystals that infill pore space
553 within the microspar (M) dolomite (Fig. 5A), and larger cavity lining crystals that exhibit patchy
554 rhombic cores in CL but not in plane polarized light (Fig. 5B). The rhombohedral cores are
555 chemically distinct from the zonation bands that outline them. The cores exhibit the same blue,
556 grey, and gold CL characteristics as the microspar and may represent penecontemporaneous
557 formation with the microspar dolomite, from the same type of fluids (Fig. 5). Additionally,
558 microspar and zoned dolomite contain trace amounts of Si (Fig. 4F) which also suggest the same
559 formation fluids for both phases. The presence of patchy cores detected in CL, but not
560 observable under plane polarized light (PPL), within some of the larger rhombic cores is not well
561 understood. Kaczmarek and Sibley (2014) suggest this pattern may be derived from
562 inhomogeneous fluids during crystal growth or recrystallization. Alternative explanations include
563 multiple dolomite dissolution-precipitation phases (Sena et al., 2014), or inclusions (Budd,
564 1997). We do not see evidence for inhomogeneous fluids from EPMA line scans, and Raman did
565 not detect any non-carbonate related peaks to explain inclusions, nor were inclusions observed
566 within the crystals. Additionally, we do not have supporting evidence for dissolution-
567 precipitation phases and therefore an interpretation based on direct evidence is not available at
568 the moment.

569 The concentric pattern of zonation, that outlines the rhombic cores, is a result of primary
570 crystal growth stages and relates to the fluctuating fluid chemistry during formation (Reeder,
571 1991; Budd, 1997). The crystal zones altered between Ca:Mg zones (light bands) and Fe:Mg
572 zones (dark bands) indicating changes in Ca, Mg and Fe concentrations in dolomitizing fluids
573 during the crystal growth (Figs. 5G, 6B). The dark bands are likely from Fe- and Mn-rich fluids
574 that periodically entered the system during dolomitization.

575 5.2.1.3. *Saddle dolomite*

576 Ongoing, deeper burial produced late stage chemical compaction from overburden pressure
577 resulting in stylolites and localized dissolution seams that are concentrated in the lagoonal facies
578 and occur throughout the outcrop (Figs. 2B, O). The second stage of microfracturing produced
579 fractures that later infilled with saddle dolomite (Fig. S5 in supplementary material). The dull
580 luminescence of saddle dolomite (S), Fe-rich chemistry, and saddle shape are all features of late
581 stage, high temperature dolomite formation (Machel, 1987; Radke and Mathis, 1980; Warren,
582 2000). Although there is no direct evidence for primary precipitation, the lack of floating
583 particles of other minerals within the crystals, and the lack of irregular and sutured crystal
584 boundaries, indicate that this is not a replacement phase (Radke and Mathis, 1980), but rather a
585 primary precipitate during burial diagenesis. Possible penecontemporaneous formation of saddle
586 dolomite and stylolites may be inferred from one crosscutting feature observed at the outcrop,
587 where an overlying stylolite seemed collapsed into a large vug and is surrounded by the infilling
588 saddle dolomite (Fig. 2Q). The saddle dolomite was likely formed in a water-buffered,
589 isotopically open, system where Fe and Mn fluids were incorporated into the dolomite along
590 with the Mg/Ca dolomitizing fluids (Budd, 1997). This final stage of burial diagenesis thermally
591 overprinted the entire formation as revealed from organic carbon Raman D and G bands and
592 previous CAI thermometry temperatures of the microspar dolomite (Table 4).

593 Based on petrographic features, CL, and EPMA, the three dolomite mineral phases are multi-
594 generational and formed over three stages (Fig. 13). The first, second, and third generations of
595 dolomite are microspar, zoned, and saddle, respectively.

596 5.2.2. *Carbonate $\delta^{18}\text{O}$ and $\delta^{13}\text{C}$ composition*

597 The low $\delta^{18}\text{O}_{\text{dolo}}$ values (-18.23‰ to -6.05‰ VPDB) reflect the deep burial diagenetic setting
598 where the saddle dolomite formed (Haas et al., 2017; Al-Aasm and Crowe, 2018), in an
599 isotopically open system and at higher temperatures than those of microspar and zoned dolomite
600 formation (Fig. 9). A comparison of $\delta^{18}\text{O}_{\text{dolo}}$ values from the micro-drilled saddle and microspar
601 dolomites shows that these values cannot be differentiated from bulk carbonate $\delta^{18}\text{O}_{\text{dolo}}$ values as
602 they fall within the range of error bars (Fig. 9). The overlap of $\delta^{18}\text{O}_{\text{dolo}}$ values in dolomite phases
603 (Fig. 9) might be explained by the formation of dolomite in an isotopically open system, or the
604 resetting of isotopes during burial diagenesis or recrystallization under high temperatures (Land,
605 1980; Malone et al., 1994; Warren, 2000; Swart, 2015). Because burial diagenesis and
606 recrystallization can result in the same signatures (Kaczmarek and Sibley, 2014), the Allentown
607 dolomite, if recrystallized, would be significantly recrystallized with respect to depleted $\delta^{18}\text{O}$,
608 and insignificantly recrystallized with respect to all other evaluated parameters (Machel, 1997).
609 However, due to burial evidence (e.g., stylolites) the depleted $\delta^{18}\text{O}$ signature is likely more
610 appropriately attributed to a burial diagenetic setting.

611 Variations in the origin of sedimentary materials and diagenesis should be taken into account
612 when interpreting the $\delta^{13}\text{C}_{\text{dolo}}$ and $\delta^{13}\text{C}_{\text{org}}$ (Swart, 2015). The low $\delta^{13}\text{C}_{\text{dolo}}$ values (e.g., -6‰
613 VPDB) can indicate thoroughly altered isotopic compositions, as a result of diagenesis in an
614 open system with high fluid:rock ratios (Lohmann, 1988; Sharp, 2007). This interpretation
615 corresponds well with findings of the saddle dolomite in the Allentown samples. In order for
616 saddle dolomite to form, the Fe and Mn-rich fluids needed to mix with the dolomitizing (Mg/Ca)
617 fluids, which requires a high fluid:rock ratio most likely found in an open system (Brand and
618 Veizer, 1980; Budd, 1997). This interpretation fits well with the Allentown $\delta^{13}\text{C}_{\text{dolo}}$ values (Fig.
619 9) and petrographic data. Alternatively, the low $\delta^{13}\text{C}_{\text{dolo}}$ values may derive from diagenetic

620 alteration of oxidized organics in the system (Irwin et al., 1977; Lohmann, 1988; Schidlowski,
621 1988; Swart, 2015). The relatively low TOC (Table S1 in supplementary material) in the
622 Allentown samples suggests that the organic signature is not likely the main, or single, influence
623 on $\delta^{13}\text{C}_{\text{dolo}}$ values.

624 Coupling of $\delta^{18}\text{O}_{\text{dolo}}$ and $\delta^{13}\text{C}_{\text{dolo}}$ isotopes suggests contemporaneous alteration from the same
625 source(s) for both $\delta^{18}\text{O}_{\text{dolo}}$ and $\delta^{13}\text{C}_{\text{dolo}}$ isotopes and all samples (Des Marais et al., 1992; Jiang et
626 al., 2012) (Fig. 10B). The decoupled trends of $\delta^{13}\text{C}_{\text{org}}$ with $\delta^{18}\text{O}_{\text{dolo}}$ and $\delta^{13}\text{C}_{\text{dolo}}$ may be related to
627 diagenetic alteration in a system that was not rock buffered and does not retain the original
628 $\delta^{13}\text{C}_{\text{dolo}}$ values (Grotzinger et al., 2011; Jiang et al., 2012; Oehlert and Swart, 2014). The
629 decoupling trend may occur due to variations in $\delta^{13}\text{C}_{\text{org}}$ values that may reflect mixed organic
630 sources and diagenesis (Swart, 2015). Alternatively, the decoupled $\delta^{13}\text{C}_{\text{org}}$ and $\delta^{13}\text{C}_{\text{dolo}}$ values
631 may imply relatively unaltered values that reflect values of the shallow water organic matter. In
632 this scenario, a lack of correlation between the two values may occur due to the wide range of
633 $\delta^{13}\text{C}$ from organic matter and a relatively narrow range in $\delta^{13}\text{C}$ from inorganic matter (Oehlert et
634 al., 2012; Swart, 2015).

635 Jiang et al. (2012) reported decoupled $\delta^{13}\text{C}_{\text{org}}$ and $\delta^{13}\text{C}_{\text{dolo}}$ in Cambrian carbonates with low
636 TOC (<0.1 wt%) and interpreted this as a result of diagenetic alteration of organic carbon,
637 amplification of detrital organic carbon isotope signature in organic-poor carbonates, or both
638 processes simultaneously. In an oxidizing setting, primary marine-derived organic carbon will
639 degrade faster than terrestrial organics, and a low TOC (<0.2 wt%) with negative $\delta^{13}\text{C}_{\text{org}}$ can
640 result (Oehlert and Swart, 2014). Evidence for various organic matter sources is supported by
641 Raman data where D and G bands cluster based on the type of carbonate deposit (stromatolite,
642 thrombolite, and oolitic) in tidal flat to shoal facies. Additionally, Lamb et al. (2006) showed that

643 the provenance of organic matter sources varies within the peritidal sequence of a coastal
644 environment. Organic sources may vary from near-shore tidal flats hosting a mix of marine and
645 terrestrial tides and river derived organics, to ooid shoals dominated by in situ marine derived
646 organic sources from isolated waters (Lamb et al., 2006). Based on the Allentown's depleted
647 isotope measurements, low TOC, high temperature and burial settings (saddle dolomite,
648 stylolites), the Allentown isotopic values are likely the result of diagenetic alteration of organic
649 carbon and a detrital organic carbon isotope signature (Jiang et al., 2012).

650 **5.3. Characterization of organic carbon**

651 Organic carbon is characterized based on TOC, $\delta^{13}\text{C}_{\text{org}}$, Confocal Raman microscopy, and D
652 and G peak analyses in order to determine spatial relationships between organic matter and
653 minerals, alteration and thermal maturity of the organic carbon.

654 *5.3.1. TOC and $\delta^{13}\text{C}_{\text{org}}$*

655 The samples with higher TOC concentrations (0.484 to 0.286 wt%) have lighter $\delta^{13}\text{C}_{\text{org}}$
656 compositions (-28.25 to -27.45‰ relative to VPDB), while samples with lower TOC (0.025 to
657 0.120 wt%) show heavier $\delta^{13}\text{C}_{\text{org}}$ compositions (-27.44 to -25.73‰ relative to VPDB) (Fig.
658 10A). Such a decrease in TOC coupled with heavier $\delta^{13}\text{C}_{\text{org}}$ values may be indicative of post-
659 depositional thermal degradation (McKirdy and Powell, 1974; Strauss and Beukes, 1996;
660 Eigenbrode and Freeman, 2006; Jiang et al., 2012). The overall TOC values for transect A are
661 relatively similar and the TOC values of transect B are varying, but the $\delta^{13}\text{C}_{\text{org}}$ values are similar
662 (Fig. 10). This TOC diversity and $\delta^{13}\text{C}_{\text{org}}$ similarity suggests that thermal degradation is not a
663 dominate factor in characterization of the organics.

664 Oolitic dolosiltite sample B9 has the highest TOC at 0.48 wt%; this sample contains rip-up
665 clasts, which are characteristic for tidal channel deposits formed during storms. High TOC

666 concentrations are also present in oolitic dolarenite samples B10, B11, and oolitic dolosiltite
667 sample B13, all of which include evidence of high energy, storm events (rip-up clasts and
668 edgewise conglomerates), which had capacity to deliver additional organic input within these
669 layers.

670 The input of terrestrial organic matter washed in during storms in supra- to inter-tidal areas
671 could had been incorporated in the sediments and stromatolitic laminae and in the thrombolites
672 during deposition and contributed to the mixed pool signatures as seen in Raman (Fig. 11B) and
673 $\delta^{13}\text{C}_{\text{org}}$ (Table S1 in supplementary material) data.

674 The measured values of $\delta^{13}\text{C}_{\text{org}}$ range from -25.73‰ to -28.25‰ relative to VPDB (Fig.
675 10B), which is broadly consistent with organic input from decaying organic matter or microbial
676 metabolism (Irwin et al., 1977; Schidlowski, 1988; Lamb et al., 2006). The lighter values of
677 oolitic samples (B transect) from the subtidal area likely reflect marine organics, while the
678 heavier values of stromatolites and thrombolites likely include a mixture of terrestrial and marine
679 organics (Torgersen and Chivas, 1985; Middelburg et al., 1997; Megens et al., 2002) (Fig. 10A,
680 Table S1 in supplementary material).

681 *5.3.2. Characterization of organic carbon based on confocal Raman spectroscopy*

682 The spatial relation of the organic carbon to multi-generational dolomite is significant for
683 determining if the carbon was already in place before dolomitization, and therefore syngenetic
684 with the Cambrian stromatolites. Confocal Raman microscopy reveals that D and G bands of
685 organic carbon are only present in the first generation of microspar dolomite and situated at or
686 near grain boundaries (Fig. 11).

687 *5.3.2.1. Raman thermometry*

688 Oxygen isotope ratios are commonly used as a geothermometer to estimate the thermal
689 history of carbonate minerals (Friedman and O’Neil, 1977; Land, 1983). However, the measured
690 oxygen isotope values in this study reflect the late burial fluids from an open system that
691 replaced the Cambrian isotopic seawater values and rendered them unusable (Land, 1980; Sharp,
692 2007).

693 The color alteration index (CAI) of conodont fossils is another method used as a
694 geothermometer for sedimentary rocks (Epstein et al., 1977; Marshall et al., 2001). Conodont
695 fossils found in Warren and Sussex counties of New Jersey Allentown outcrops have CAI
696 (Epstein et al., 1977; Helsen et al., 1995) values of five indicating temperatures of at least 300°C
697 and burial depths of at least 10 km (Harris et al., 1995). Burial depths around 10 km would
698 correspond to burial pressure of at least 300 MPa (Tilley, 1924). Based on our outcrop
699 observations and microtextural evidence, this outcrop had not been exposed to unidirectional
700 stress that would align or elongate grains, but the pressure was likely lithostatic and uniform
701 pressure derived from the burial process.

702 Calculated temperatures from Raman data yield a range 260 - 322°C ($\pm 30^\circ\text{C}$) for the
703 Allentown organic carbon (Table 4). This type of organic carbon alteration is also reflected in the
704 overall D and G band spectral characteristics, which exhibit D3 and D4 bands, and commonly
705 have D and G bands that are equal in intensity (Table 3, Tables S3a, S3b in supplementary
706 material). These newly calculated temperatures based on Raman data corroborate previously
707 estimated temperatures based on conodont fossil CAI values.

708 Within the newly derived temperatures, two distinct groups of organic carbon differentiate
709 (Table 4) stromatolite (A16) and oolitic samples (A7, B11, B12a) exhibit higher temperatures
710 that average 314°C ($\pm 30^\circ\text{C}$) compared to thrombolite (A5) samples that average 271°C ($\pm 30^\circ\text{C}$).

711 The D1 band positions, and associated temperatures are statistically different ($p<0.05$) between
712 these rock types (Figs. S1b, S2 in supplementary material). Variations in D1 band characteristics
713 between facies may be related to different types of initial organic matter (e.g., marine vs
714 terrestrial), because the temperatures do not correlate with strata depth. For example,
715 thrombolites record the lowest temperatures, while the stromatolites, which are coeval to or
716 younger than thrombolites (Figs. 1C, 3), have higher average temperatures. The clear
717 interpretation of these temperature differences is not attainable at the moment; however, based
718 on the fact that they are separated as different facies, we may assume that different types of
719 initial organic material contained in different facies may have altered differently despite the same
720 diagenetic setting (Wopenka and Pasteris, 1993).

721 Other factors that may influence micron-scale variation of organic carbon include differential
722 shear deformation (Bustin et al., 1995), artifacts from sample polishing (Beyssac et al., 2003),
723 and mineral templating effects (van Zuilen et al., 2012). In this study, there is no evidence of
724 shear stress or strain (i.e., grains are randomly oriented) and Raman spectra was taken beneath
725 the sample surface to avoid polishing effects on carbon material. Additionally, dolomitization
726 was pervasive and uniformly affected the organic carbon that is limited to the first generation of
727 dolomite (microspar). The organic carbon in this study is not coating the grains as seen in
728 mineral templating due to matrix effects in quartz matrix samples (e.g., van Zuilen et al., 2012)
729 but rather situated between dolomite grain boundaries which is expected for organic material in
730 carbonate rocks when trapped between grains during sediment lithification and mineral growth.
731 The Raman heterogeneity observed in individual mapped areas of these samples (Fig. 11B-C) is
732 therefore not caused by any known factors related to secondary geologic processes (i.e.,

733 diagenesis or metamorphism) and is likely due to primary biological variation related to
734 variations from the original organic starting material (Foucher et al., 2015; Qu et al., 2015).

735 *5.4. Organic carbon origins*

736 Based on the spatial distribution and exclusive occurrence of organic material in the
737 replacive microspar dolomite, it is very possible that the organic carbon was trapped in the
738 samples during original limestone lithification, and thus was already in place during
739 dolomitization (Fig. 11A, Figs. S8aC-E in supplementary material). This early dolomitization
740 likely occurred from seawater supersaturated in Mg ions, that rapidly produced stoichiometric
741 dolomite, a thermodynamically stable phase (Carpenter, 1980; Nordeng and Sibley, 1994;
742 Mueller et al., 2019), which resisted further alteration during burial diagenesis and preserved the
743 Cambrian organics. The placement of organic carbon suggests it is indigenous and syngenetic to
744 the primary fabric of the host rock. The Raman cluster maps show the peak variations overlap
745 spatially within the same mapped area (Fig. 11B, Figs. S8aC-E in in supplementary material),
746 suggesting all three varieties of organics were in place at the same time, matching the alteration
747 temperature of the host rock.

748 Claims of biogenicity for organic carbon that is not associated with cellular morphological
749 evidence should be approached with caution. The finding of organic carbon with an isotopic
750 composition that may be indicative of microbial metabolism is not an explicit line of evidence
751 for biogenicity (Braiser et al., 2004; De Gregorio and Sharp, 2006). Organic molecules can form
752 from abiotic, autochthonous chemical reactions such as Fischer-Tropsch type processes in
753 hydrothermal environments and decarbonation during metamorphism (McCollom and Seewald,
754 2006; Galvez et al., 2013; Bernard and Papineau, 2014). Although this null hypothesis cannot be
755 fully rejected, there is no evidence of such hydrothermal processes in the outcropping area.

756 Evidence supporting a biogenic origin for Allentown organic carbon includes: (1) organic
757 carbon is exclusive to the primary fabric (microspar dolomite) of the host rock which indicates a
758 syngenetic origin, (2) the geological context is a marginal-marine setting that is a favorable
759 habitat to marine organisms and overall rich in biological organic material, and one of the
760 obvious sources of organics are numerous microbial stromatolite macrostructures observed at the
761 outcrop, and (3) geochemical signals of $\delta^{13}\text{C}_{\text{org}}$ values are consistent with decaying organic
762 matter or microbial metabolism (Irwin et al., 1977; Schidlowski, 1988; Lamb et al., 2006).
763 Although the detection of disordered carbon by Raman spectroscopy is not alone indicative of
764 biogenicity (Pasteris and Wopenka, 2003), the combined petrographic, sedimentary, and
765 geochemical evidence from Allentown organic carbon supports a biogenic origin.

766 The degree of crystallinity in carbonaceous matter is affected by the type of organic matter
767 and host rock composition during heating (Wopenka and Pasteris, 1993), therefore the D and G
768 peak differences may be due to different types of organic starting material that altered, or
769 decomposed, differently despite the same alteration setting (Lamb et al., 2006). The peak shifts
770 in D and G band positions within the same mapped area (e.g., Fig. 11C) is indicative of three
771 differently altered organic carbon molecules, which suggests different source pools of indigenous
772 and syngenetic organic material. Lamb et al. (2006) reported organic matter in Holocene
773 lagoonal and tidal flat sediments is mostly derived from suspended particulate organic matter
774 such as plant detritus and phytoplankton from river and marine sources, respectively. This
775 variation in tidal flat organics may potentially explain how three phases of organic carbon are
776 found in the stromatolite and thrombolite samples (A16 and A5, respectively), while oolitic (A7,
777 B11 and B12a) samples only have one carbon phase present (Fig. 11E, S8a in supplementary
778 material). Since no nitrogen was detected by IRMS, characterization of organic sources based on

779 C/N ratios (e.g., Lamb et al., 2006) is not possible. Instead, using the $\delta^{13}\text{C}_{\text{org}}$ values alone show
780 an overlap of marine and freshwater organic carbon (Lamb et al., 2006).

781

782 **6. CONCLUSIONS**

783 Traditionally, secondary, stoichiometric, and ordered dolomite has been hypothesized to
784 occur at either high temperatures or from multiple stages of recrystallization (Machel, 1978;
785 Kupecz et al., 1993; Gregg et al., 2015) that would likely erase evidence of original texture,
786 chemistry, and biology (Gregg and Sibley, 1984; Grotzinger and Knoll, 1999; Schopf, 1999;
787 Warren, 2000). The results presented here indicate that stoichiometric and ordered dolomite can
788 form within early dolomitization settings, undergo increasing temperature and burial diagenesis,
789 and still retain syngenetic organic carbon. In summary:

- 790 • Outcrop scale observations (mudcracks, collapse breccia, rip-up clasts and edgewise
791 conglomerates) and petrological microtextures characteristics (finely-laminated stromatolites,
792 fenestral porosity, rip-up clasts, finely crystalline microspar dolomite) reveal that the
793 Allentown depositional setting was a tidal flat along the Cambrian coastline where original
794 calcium carbonate mineral precursors dolomitized early in a marginal marine setting.
- 795 • Bulk dolomite varies in cationic ordering from poorly to well ordered, and the stoichiometry
796 varies from low Ca-excess to stoichiometric to low Mg-excess. Individual phases of dolomite
797 are stoichiometric (microspar and zoned) and Ca-enriched (saddle).
- 798 • Geochemical characteristics recorded by each phase of dolomite suggest two dolomitization
799 processes dominated: early dolomitization in the marginal marine setting and late
800 dolomitization from deep burial diagenesis.

801 • Microspar and zoned dolomite phases formed by dolomitization in high Mg/Ca fluids,
802 resulting in finely crystalline replacive dolomite crystals, and the preservation of primary
803 depositional features such as fenestral porosity. Saddle dolomite formed by burial
804 dolomitization as revealed by coarse void-filling crystals, dull luminescence, Fe and Mn
805 enrichment, and low $\delta^{18}\text{O}_{\text{dolo}}$ values.

806 • Burial diagenesis likely thermally overprinted the microspar and zoned dolomite, as revealed
807 by Raman thermometry.

808 • Raman D and G bands indicate greenschist-like thermal maturity of organic carbon within
809 the formation which is in agreement with conodont fossil CAI geothermometry previously
810 reported for the Allentown dolostone.

811 • Organic carbon is found at or near grain boundaries, exclusively within the first generation of
812 microspar dolomite. This suggests the organics were in place when the grains of dolomite
813 formed, indicating indigenous and syngenetic origins of the organic carbon within the
814 Cambrian stromatolites.

815 • Identification by Raman spectroscopy of various pools of organic carbon was found in
816 stromatolite, thrombolite, and oolitic deposits indicating that indigenous and syngenetic
817 organic matter can be identified in many dolomitized facies.

818 This work shows that biosignature (e.g., organic carbon) preservation in carbonate environments
819 extends beyond obvious microbial structures (e.g. stromatolites and thrombolites) and may also
820 be preserved in shallow water environments that were rich in microbial life (e.g., coastal,
821 marginal marine environments). This type of research is especially important when searching for
822 life on other planets because microbial fossil preservation on Earth is rare, and different geologic
823 environments and evolutionary histories on other planetary bodies will likely result in different

824 signatures for life. Terrestrial analogs such as this study will allow for better interpretations of
825 potential biosignatures in Martian carbonates, which may have undergone varying levels of
826 alteration. Based on the data presented in this paper, the textural and mineralogical evidence that
827 may be indicative of life and biosignature preservation in carbonate environments is not limited
828 to silicified carbonates or obvious microbial structures (stromatolites), but extends to dolomitized
829 carbonates and general shallow water settings, where fine-grained carbonate minerals indicate
830 primary environments that are capable of preserving indigenous and syngenetic organic carbon.
831 The Mars Perseverance rover has the ability to target fine-grained carbonate rock, such as the
832 microspar dolomite in this study, for Raman analysis, and if carbon is detected, these may serve
833 as high potential biosignatures to be cached for future sample return mission(s).

834 **ACKNOWLEDGMENTS**

835 We are grateful to Alexander Gates and Michael Kalcynski for their assistance with field trip
836 logistics and sample collection. This study was funded by NASA ASTEP (NNX14AT28G to
837 M.G.) and NASA NAI ENIGMA – Rutgers University (80NSSC18M0093). We thank Editor-in-
838 Chief Jasper Knight and the anonymous reviewers for detailed reviews and constructive
839 comments which improved this manuscript.

840

841 **DATA AVAILABILITY**

842 Supplementary data related to this article can be found at
843 <http://dx.doi.org/10.17632/k57gbw78d9.4>, hosted at Mendeley Data (Murphy et al., subm).

844

845 **REFERENCES**

846 Al-Aasm, I.S., Crowe, R., 2018. Fluid compartmentalization and dolomitization in the Cambrian
847 and Ordovician successions of the Huron Domain, Michigan Basin. *Mar. Petrol. Geol.* 92,
848 160-178.

849 Allan, J.R., Wiggins, W.D., 1993. Dolomite reservoirs: geochemical techniques for evaluating
850 origin and distribution, AAPG Continuing Education Course Notes 36. American
851 Association of Petroleum Geologists, Tulsa, OK. 129 pp.

852 Allwood, A.C., Walter, M.R., Kamber, B.S., Marshall, C.P., Burch, I.W., 2006. Stromatolite reef
853 from the Early Archaean era of Australia. *Nature* 441, 714-718.

854 Ayllón-Quevedo, F., Souza-Egipsy, V., Sanz-Montero, M.E., Rodríguez-Aranda, J.P., 2007.
855 Fluid inclusion analysis of twinned selenite gypsum beds from the Miocene of the Madrid
856 basin (Spain). Implication on dolomite bioformation. *Sed. Geol.* 201, 212-230.

857 Barghoorn, E.S., Tyler, S.A., 1965. Microorganisms from the Gunflint Chert: These structurally
858 preserved Precambrian fossils from Ontario are the most ancient organisms known. *Science*
859 147, 563-75.

860 Bartley, J.K., Knoll, A.H., Grotzinger, J.P., Sergeev, V.N., 2000. Lithification and fabric genesis
861 in precipitated stromatolites and associated peritidal carbonates, Mesoproterozoic Billyakh
862 Group, Siberia. In: Grotzinger, J. P., James, M.P. (Eds.), *Carbonate Sedimentation and*
863 *Diagenesis in the Evolving Precambrian World*. SEPM Spec. Publ. 67, pp. 59-73.

864 Bernard, S., Papineau, D., 2014. Graphitic Carbons and Biosignatures. *Elements* 10, 435-440.

865 Beyssac, O., Goffe, B., Chopin, C., Rouzaud, J. N., 2002. Raman spectra of carbonaceous
866 material in metasediments: a new geothermometer. *J. Metamorphic Geol.* 20, 859-871.

867 Beyssac, O., Goffe, B., Petitet, J., Froigneux, E., Moreau, M., Rouzaud, J.N., 2003. On the
868 characterization of disordered and heterogeneous carbonaceous materials by Raman
869 spectroscopy. *Spectrochim. Acta A Mol. Biomol. Spectrosc.* 59, 2267–2276.

870 Blakey, R., 2016. Global Paleogeography and Tectonics in Deep Time Series. Colorado Plateau
871 Geosystems Inc. [https://deeptimemaps.com/wp-](https://deeptimemaps.com/wp-content/uploads/2016/05/500_ma_Cambrian_GPT-1.png)
872 [content/uploads/2016/05/500_ma_Cambrian_GPT-1.png](https://deeptimemaps.com/wp-content/uploads/2016/05/500_ma_Cambrian_GPT-1.png) (Accessed 6 July 2020).

873 Bragg, W.H., Bragg W.L., 1913. The Reflection of X-rays by Crystals. *Proceedings of the Royal*
874 *Society of London. Series A, Containing Papers of a Mathematical and Physical Character*
875 88, 428-438.

876 Braiser, M., Green, O., Lindsay, J., Steele, A., 2004. Earth's oldest (~3.5 Ga) Fossils and the
877 'Early Eden Hypothesis': Questioning the Evidence. *Origins Life Evol. Biosphere* 34, 257-
878 269.

879 Braiser, M.D., Antcliffe, J., Saunders, M., Wacey, D., 2015. Changing the picture of Earth's
880 earliest fossils (3.5–1.9 Ga) with new approaches and new discoveries. *PNAS* 112, 4859-
881 4864.

882 Brand, U., Veizer, J., 1980. Chemical Diagenesis of a Multicomponent Carbonate System – 1:
883 Trace Elements. *J. Sediment. Petrol.* 50, 1219-1236.

884 Budd, D.A., 1997. Cenozoic dolomites of carbonate islands: their attributes and origin. *Earth-*
885 *Science Reviews* 42, 1-47.

886 Buick, R., 1990. Microfossil Recognition in Archean Rocks: An Appraisal of Spheroids and
887 Filaments from a 3500 M.Y. Old Chert-Barite Unit at North Pole, Western Australia. *Palaios*
888 5, 441-459.

889 Buie, B.F., 1932. A Report of Investigations of the Allentown Limestone Formation(Master's
890 thesis). LeHigh University, PA.

891 Bustin, R.M., Ross, J.V., Rouzaud, J.N., 1995. Mechanisms of graphite formation from kerogen:
892 experimental evidence. *Int. J. Coal Geol.* 28, 1-36.

893 Cady, S.L., Farmer, J.D., Grotzinger, J.P., Schopf, J.W., Steele, A., 2003. Morphological
894 Biosignatures and the Search for Life on Mars. *Astrobiology* 3, 351-368.

895 Carpenter, A.B., 1980. The chemistry of dolomite formation I: the stability of dolomite. In:
896 Zenger, D.H., Dunham, J.B., Ethington, R.L. (Eds.), *Concepts and Models of Dolomitization.*
897 *Spec. Publ. Soc. Econ. Paleont. Miner.* 28, pp. 11-122.

898 Calça, C.P., Fairchild, T.R., Cavalazzi, B., Hachiro, J., Petri, S., Huila, M.F.G., Toma, H.E.,
899 Araki, K., 2016. Dolomitized cells within chert of the Permian Assistência Formation, Paraná
900 Basin, Brazil. *Sediment. Geol.* 335, 120-135.

901 Dalton, R.F., Volkert, R.A., Monteverde, D.H., Herman, G.C., Canace, R.J., 2014. Bedrock
902 Geologic Map of the Hamburg Quadrangle, Sussex County, New Jersey (1:24,000). New
903 Jersey Geological and Water Survey, Trenton, NJ.

904 De Gregorio, B.T., Sharp, T.G., 2006. The structure and distribution of carbon in 3.5 Ga Apex
905 chert: Implications for the biogenicity of Earth's oldest putative microfossils. *Amer. Miner.*
906 91, 784-789.

907 D'Elia, M., Blanco, A., Galiano, A., Orofino, V., Fonti, S., Mancarella, F., Guido, A., Russo, F.,
908 Mastandrea, A., 2017. SEM morphological studies of carbonates and the search for ancient
909 life on Mars. *Int. J. Astrobiology* 16, 137-142.

910 Des Marais, D.J., Strauss, H., Summons, R.E., Hayes, J.M., 1992. Carbon isotope evidence for
911 the stepwise oxidation of the Proterozoic environment. *Nature* 359, 605-609.

912 Dong, L., Shen, B., Lee, C.A., Shu, X., Peng, Y., Sun, Y., Tang, Z., Rong, H., Lang, X., Ma, H.,
913 Yang, F., Guo, W., 2015. Germanium/silicon of the Ediacaran-Cambrian Laobao cherts:
914 Implications for the bedded chert formation and paleoenvironment interpretations. *Geochem.*
915 *Geophys. Geosyst.* 16, 751-763.

916 Drake Jr., A.A., 1965. Carbonate Rocks of Cambrian and Ordovician Age Northampton and
917 Bucks Counties, Eastern Pennsylvania and Warren and Hunterdon Counties, Western New
918 Jersey. *Bull. US Geol. Surv.* 1194-L, 12 pp.

919 Eigenbrode, J.L., Freeman, K.H., 2006. Late Archean rise of aerobic microbial ecosystems.
920 *PNAS* 103, 15759-15764.

921 Epstein, A.G., Epstein, J.B., Harris, L.D., 1977. Conodont Color Alteration – an Index to
922 Organic Metamorphism. *US Geol. Surv. Professional Paper* 995.

923 Flügel, E., 2004. Carbonate Depositional Environments. In: Flügel, E. (Ed.), *Microfacies of*
924 *Carbonate Rocks*. Springer, Berlin, Heidelberg, pp. 7-52.

925 Folk, R.L., 1959. Practical petrographic classification of limestones. *Bull. Amer. Assoc. Petrol.*
926 *Geol.* 43, 1-38.

927 Foucher, F., Ammar, M.R., Westall, F., 2015. Revealing the biotic origin of silicified
928 Precambrian carbonaceous microsignatures using Raman spectroscopic mapping, a potential
929 method for the detection of microfossils on Mars. *J. Raman Spectrosc.* 46, 873-879.

930 Friedman, I., O’Neil, J.R., 1977. Compilation of stable isotope fractionation factors of
931 geochemical interest. *US Geol. Surv. Professional Paper* 440-KK, 11 pp.

932 Galvez, M.E., Beyssac, O., Martinez, I., Benzerara, K., Chaduteau, C., Malvoisin, B.,
933 Malavieille, J., 2013. Graphite formation by carbonate reduction during subduction. *Nature*
934 *Geoscience* 6, 473-477.

935 Gasparrini, M., Bechstädt, T., Boni, M., 2006. Massive hydrothermal dolomites in the
936 southwestern Cantabrian Zone (Spain) and their relation to the Late Variscan evolution. Mar.
937 Petrol. Geol. 23, 543–568.

938 Goldsmith, J.R., Graf, D.L., 1958. Relation between lattice constants and composition of the Ca-
939 Mg carbonate. Am. Mineral. 43, 84-101.

940 Graf, D.L., Goldsmith, J.R., 1956. Some Hydrothermal Syntheses of Dolomite and
941 Protodolomite. J. Geol. 64, 173-186.

942 Gregg, J.M., Bish, D.L., Kaczmarek, S.E., Machel, H.G., 2015. Mineralogy, nucleation and
943 growth of dolomite in the laboratory and sedimentary environment: A review. Sedimentology
944 62, 1749-1769.

945 Gregg, J.M., Sibley, D.F., 1984. Epigenetic dolomitization and the origin of xenotopic dolomite
946 texture. J. Sediment. Petrol. 54, 908-931.

947 Grotzinger, J.P., Rothman, D.H., 1996. An abiotic model for stromatolite morphogenesis. Nature
948 383, 423-425.

949 Grotzinger, J.P., Knoll, A.H., 1999. Stromatolites in Precambrian Carbonates: Evolutionary
950 Mileposts or Environmental Dipsticks? Annu. Rev. Earth Planet. Sci. 27, 313-358.

951 Grotzinger, J.P., Fike, D.A., Fischer, W.W., 2011. Enigmatic origin of the largest-known carbon
952 isotope excursion in Earth's history. Nat. Geosci. 4, 285-292.

953 Guido, A., Russo, F., Miriello, D., Mastandrea, A., 2018. Autochthonous Micrite to
954 Aphanodolomite: The Microbialites in the Dolomitization Process, Geosciences 8, 451.
955 <https://doi.org/10.3390/geosciences8120451>.

956 Haas, J., Hips, K., Bundai, T., Gyori, O., Lukoczki, G., Kele, S., Demeny, A., Poros, Z., 2017.

957 Processes and controlling factors of polygenetic dolomite formation in the Transdanubian

958 Range, Hungary: a synopsis. *Int. J. Earth Sci.* 106, 991-1021.

959 Habermann, D., Götze, J., Neuser, R., Richter, D.K., 1997. The phenomenon of intrinsic

960 cathodoluminescence: Case studies of quartz, calcite and apatite. *Zentralbl Geol Paläont Teil*

961 1, Heft 10–12, 1275–1284.

962 Harris, A.G., Repetski, J.E., Stamm, N.R., Weary, D.J., 1995. Conodont Age and CAI Data for

963 New Jersey. *US Geol. Surv. Open-File Report 95-557*, 32 pp.

964 Helsen, S., David, P., Fermont, W.J.J., 1995. Calibration of Conodont Color Alteration Using

965 Color Image Analysis. *J. Geol.* 103, 257-267.

966 Hips, K., Haas, J., Poros, Z., Kele, S., Budai, T., 2015. Dolomitization of Triassic microbial mat

967 deposits (Hungary): Origin of microcrystalline dolomite. *Sed. Geol.* 318, 113-129.

968 Hoffman, H.J., 2013. Archean Stromatolites as Microbial Archives. In: Riding, R.E., Awramik,

969 S.M., (Eds.), *Microbial Sediments*, Springer, Springer Berlin Heidelberg, pp. 315-327.

970 Horgan, B.H.N., Anderson, R.B., Dromart, G., Amador, E.S., Rice, M.S., 2020. The mineral

971 diversity of Jezero crater: Evidence for possible lacustrine carbonates on Mars. *Icarus* 339,

972 113526. <https://doi.org/10.1016/j.icarus.2019.113526>.

973 Howell, B.F., 1945. Revision of Upper Cambrian faunas of New Jersey. *Geological Society of*

974 *America, Memoir 12*, 1355-1368.

975 Irwin, H., Curtis, C., Coleman, M., 1977. Isotopic evidence for source of diagenetic carbonates

976 formed during burial of organic-rich sediments. *Nature* 269, 209-213.

977 Jiang, G., Wang, X., Shi, X., Xiao, S., Zhan, S., Dong, J., 2012. The origin of decoupled
978 carbonate and organic carbon isotope signatures in the early Cambrian (ca. 542-520 Ma)
979 Yangtze platform. *Earth Planet Sci Lett.* 317-318, 96-110.

980 Jiang, W., Hou, M., Wang, C., 2019. Strontium isotopic compositions of Cambrian (Upper
981 Miaolingian-Furongian Series) dolomites from south-eastern Sichuan Basin, China:
982 Significance of sources of dolomitizing fluids and timing of dolomitization. *Mar. and Petrol.*
983 *Geol.* 109, 408-418.

984 Kaczmarek, S.E., Sibley, D.F. 2011. On the evolution of dolomite stoichiometry and cation order
985 during high-temperature synthesis experiments: An alternative model for the geochemical
986 evolution of natural dolomites. *Sed. Geol.* 240, 30-40.

987 Kaczmarek, S.E., Sibley, D.F., 2014. Direct physical evidence of dolomite recrystallization.
988 *Sedimentology* 61, 1862-1882.

989 Knoll, A.H., Strother, P.K., Rossi, S., 1988. Distribution and Diagenesis of Microfossils from the
990 Lower Proterozoic Duck Creek Dolomite, Western Australia. *Precambr. Res.* 38, 257-279.

991 Kouketsu, Y., Mizukami, T., Mori, H., Endo, S., Aoya, M., Hara, H., Nakamura, D., Wallis, S.,
992 2014. A new approach to develop the Raman carbonaceous material geothermometer for
993 low-grade metamorphism using peak width. *Island Arc* 23, 33-50.

994 Kupecz, J.A., Montanez, I.P., Gao, G., 1993. Recrystallization of Dolomite with Time. In:
995 Rezak, R., Lavoie, D.L. (Eds.), *Carbonate Microfabrics. Frontiers in Sedimentary Geology.*
996 Springer, New York, NY, pp 187-193.

997 Lamb, A.L., Wilson, G.P., Leng, M.J., 2006. A review of coastal palaeoclimate and relative sea-
998 level reconstructions using $\delta^{13}\text{C}$ and C/N ratios in organic material. *Earth Sci. Rev.* 75, 29-
999 57.

1000 Land, L.S., 1980. The isotopic and trace element geochemistry of dolomite: The state of the art.

1001 In: Zenger, D.H., Dunham, J.B., Ethington, R.L. (Eds.), Concepts and Models of

1002 Dolomitization. SEPM Spec. Publ. 28, pp. 87-110.

1003 Land, L.S., 1983. The Application of Stable Isotopes to Studies of the Origin of Dolomite and to

1004 Problems of Diagenesis of Clastic Sediments. In: Arthur, M.A. (Ed.), Stable Isotopes in

1005 Sedimentary Geology. SEPM Short Course 10, pp.1-22.

1006 Lindtke, J., Ziegenbalg, S.B., Brunner, B., Rouchy, J.M., Pierre, C., Peckmann, J., 2011.

1007 Authigenesis of native sulphur and dolomite in a lacustrine evaporitic setting (Hellín basin,

1008 Late Miocene, SE Spain). *Geol. Mag.* 148, 655-669.

1009 Lohmann, K.C., 1988. Geochemical patterns of meteoric diagenetic systems and their application

1010 to studies of paleokarst. In: James, N.P., Choquette, P.W. (Eds.), *Paleokarst*. Springer-

1011 Verlag, New York, pp. 58–80.

1012 Lukoczki, G., Haas, J., Gregg, J.M., Machel, H.G., Kele, S., John, C.M., 2020. Early

1013 dolomitization and partial burial recrystallization: a case study of Middle Triassic peritidal

1014 dolomites in the Villany Hills (SW Hungary) using petrography, carbon, oxygen, strontium

1015 and clumped isotope data. *Int. J. Earth Sci.* 109, 1051-1070.

1016 Lumsden, D.N., 1979. Discrepancy between thin-section and X-ray estimates of dolomite in

1017 limestone. *J. Sed. Petrol.* 49, 429-436.

1018 Machel, H.G., 1978. Dolomites and dolomitization. In: *Sedimentology. Encyclopedia of Earth*

1019 *Science*. Springer, Berlin, Heidelberg. pp. 234-243.

1020 Machel, H.G., 1987. Saddle dolomite as a by-product of chemical compaction and

1021 thermochemical sulfate reduction. *Geology* 15, 936-940.

1022 Machel, H.G., 1997. Recrystallization versus neomorphism, and the concept of 'significant
1023 recrystallization' in dolomite research. *Sed. Geol.* 113, 161-168.

1024 Machel, H.G., 2004. Concepts and models of dolomitization – a critical reappraisal. In:
1025 Braithwaite, C.J.R., Rizzi, G., Darke, G. (Eds.), *The Geometry and Petrogenesis of Dolomite*
1026 *Hydrocarbon Reservoirs*. Geol. Soc. London, Spec. Publ. 235, pp. 7-63.

1027 Machel, H.G., Mason, R.A., Mariano, A.N., Mucci, A., 1991. Causes and Emission of
1028 Luminescence in Calcite and Dolomite. In: Barker, C.E., Kopp, O.C. (Eds.), *Luminescence*
1029 *Microscopy and Spectroscopy: Qualitative and Quantitative Applications*. SEPM Short
1030 Course Notes 25, pp. 9-25.

1031 MacNaughton, R.B., Hagadorn, J.W., Dott Jr., R.H., 2019. Cambrian wave-dominated tidal-flat
1032 deposits, central Wisconsin, USA. *Sedimentology* 66, 1643-1672.

1033 Marshall, A.O., Emry, J.R., Marshall, C.P., 2012. Multiple Generations of Carbon in the Apex
1034 Chert and Implications for Preservation of Microfossils. *Astrobiology* 12, 160-166.

1035 Marshall, C.P., Mar, G.L., Nicoll, R.S., Wilson, M.A., 2001. Organic geochemistry of artificially
1036 matured conodonts. *Org. Geochem.* 32, 1055-1071.

1037 McCollom, T.M., Seewald, J.S., 2006. Carbon isotope composition of organic compounds
1038 produced by abiotic synthesis under hydrothermal conditions. *Earth Planet Sci Lett.* 243, 74-
1039 84.

1040 McKirdy, D.M., Powell, T.G., 1974. Metamorphic Alteration of Carbon Isotopic Composition in
1041 Ancient Sedimentary Organic Matter: New Evidence from Australia and South Africa.
1042 *Geology* 2, 591-595.

1043 Megens, L., van der Plicht, J., de Leeuw, J.W., Smedes, F., 2002. Stable carbon and radiocarbon
1044 isotope compositions of particle size fractions to determine origins of sedimentary organic
1045 matter in an estuary. *Org. Geochem.* 33, 945-952.

1046 Middelburg, J.J., Nieuwenhuize, J., Lubberts, R.K., van de Plassche, O., 1997. Organic carbon
1047 isotope systematics of coastal marshes. *Estuar. Coast. Shelf Sci.* 45, 681-687.

1048 Miller, B.L., 1941. LeHigh County Pennsylvania: Geology and Geography, Pennsylvania
1049 Geological Survey Bulletin, 4th Series C 39. Harrisburg, PA.

1050 Monteverde, D.H., 1992. Bedrock geologic map of Sussex County, New Jersey, portions of the
1051 Culvers Gap and Lake Maskenozha quadrangles, New Jersey Geological Survey Geologic
1052 Map, 92-1.

1053 Moore, C.H., 1989. Carbonate Diagenesis and Porosity. In: Moore, C.H. (Ed.), *Developments in*
1054 *Sedimentology* 46, Amsterdam, Elsevier, pp. 46-338.

1055 Morrow, D.W., 1982. Diagenesis II. Dolomite—Part II: Dolomitization Models and Ancient
1056 Dolostones. *Geoscience Canada* 9, 95-107.

1057 Mueller, M., Igbokwe, O.A., Walter, B., Pederson, C.L., Riechelmann, S., Richter, D.K., Albert,
1058 R., Gerdes, A., Buhl, D., Neuser, R.D., Bertotti, G., Immenhauser, A., 2019. Testing the
1059 preservation potential of early diagenetic dolomites as geochemical archives. *Sedimentology*
1060 67, 849-881.

1061 Mustard, J.F., Adler, M., Allwood, A., Bass, D.S., Beaty, D.W., Bell III, J.F., Brinckerhoff, W.
1062 B., Carr, M., Des Marais, D.J., Drake, B., Edgett, K.S., Eigenbrode, J., Elkins-Tanton, L.T.,
1063 Grant, J.A., Milkovich, S.M., Ming, D., Moore, C., Murchie, S., Onstott, T.C., Ruff, S.W.,
1064 Sephton, M.A., Steele, A., Treiman, A., 2013. Report of the Mars 2020 Science Definition

1065 Team, 154 pp., posted July 2013, by the Mars Exploration Program Analysis Group
1066 (MEPAG) at http://mepag.jpl.nasa.gov/reports/MEP/Mars_2020_SDT_Report_Final.pdf.

1067 Nordeng, S.H., Sibley, D.F., 1994. Dolomite stoichiometry and Ostwald's Step Rule. *Geochim.*
1068 *Cosmochim. Acta* 58, 191-196.

1069 Oehlert, A.M., Lamb-Wozniak, K.A., Devlin, Q.B., Mackenzie, G.J., Reijmer, J.J.G., Swart,
1070 P.K., 2012. The stable carbon isotopic composition of organic material in platform derived
1071 sediments: implications for reconstructing the global carbon cycle. *Sedimentology* 59, 319-
1072 335.

1073 Oehlert, A.M., Swart, P.K., 2014. Interpreting carbonate and organic carbon isotope covariance
1074 in the sedimentary record. *Nat. Commun.* 5, 4672. <https://doi.org/10.1038/ncomms5672>.

1075 Pasteris, J.D., Wopenka, B., 1991. Raman spectra of graphite as indicators of degree of
1076 metamorphism. *Can. Mineral.* 20, 1-9.

1077 Pasteris, J.D., Wopenka, B., 2003. Necessary, but not sufficient: Raman identification of
1078 disordered carbon as a signature of ancient life. *Astrobiology* 3, 727-38.

1079 Pina, C.M., Pimentel, C., Crespo, A., 2020. Dolomite cation order in the geological record.
1080 *Chem. Geol.* 547, 119667.

1081 Plummer, P.S., Gostin, V.A., 1981. Shrinkage cracks: desiccation or synaeresis. *J. Sediment.*
1082 *Petrol.* 51, 147-1156.

1083 Pratt, B.R., James, N.P., Cowan, C.A., 1992. Peritidal carbonates. In: Walker, R.G., James, N.P.
1084 (Eds.), *Facies Models – Response to Sea Level Change*. Geological Association of Canada,
1085 pp. 303-322.

1086 Qu, Y., Engdahl, A., Zhu, S., Vajda, V., McLoughlin, N., 2015. Ultrastructural Heterogeneity of
1087 Carbonaceous Material in Ancient Cherts: Investigating Biosignature Origin and
1088 Preservation. *Astrobiology* 15, 825-842.

1089 Radke, B.M., Mathis, R.L., 1980. On the Formation and Occurrence of Saddle Dolomite. *J.*
1090 *Sediment. Petrol.* 50, 1149-1168.

1091 Ramseyer, K., Amthor, J.E., Matter, A., Pettke, T., Wille, M., Fallick, A.E., 2013. Primary silica
1092 precipitate at the Precambrian/Cambrian boundary in the South Oman Salt Basin, Sultanate
1093 of Oman. *Mar. Petrol. Geol.* 39, 187-197.

1094 Rao, V.P., Kessarkar, P.M., Krumbein, W.E., Krajewski, K.P., Schneider, R.J., 2003. Microbial
1095 dolomite crusts from the carbonate platform off western India. *Sedimentology* 50, 819-830.

1096 Reeder, R.J., 1991. An Overview of Zoning in Carbonate Minerals. In: Barker, C.E., Kopp, O.C.
1097 (Eds.), *Luminescence Microscopy and Spectroscopy: Qualitative and Quantitative*
1098 *Applications*. SEPM Short Course Notes 25, pp. 77-82.

1099 Reeder, R.J., Sheppard, C.E., 1984. Variation of lattice parameters in some sedimentary
1100 dolomites. *Am. Mineral.* 69, 520-527.

1101 Richter, D.K., Götte, T., Götze, J., Neuser, R.D., 2003. Progress in application of
1102 cathodoluminescence (CL) in sedimentary petrology. *Mineral. Petrol.* 79, 127-166.

1103 Ryan, B.H., Kaczmarek, S.E., Rivers, J.M., 2020. Early and pervasive dolomitization by near-
1104 normal marine fluids: New lessons from an Eocene evaporative setting in Qatar.
1105 *Sedimentology* 67, 2917-2944.

1106 Sanz-Montero, M.E., Rodríguez-Aranda, J.P., García del Cura, M.A., 2008. Dolomite-silica
1107 stromatolites in Miocene lacustrine deposits from the Duero Basin, Spain: the role of
1108 organotemplates in the precipitation of dolomite. *Sedimentology* 55, 729-750.

1109 Schidlowski, M., 1988. A 3,800-million-year isotopic record of life from carbon in sedimentary
1110 rocks. *Nature* 333, 313-318.

1111 Schopf, J.W., 1999. *Cradle of Life: The Discovery of Earth's Earliest Fossils*. Princeton
1112 University Press, Princeton, New Jersey, 367 pp.

1113 Schopf, J.W., Kudryavtsev, A.B., 2012. Biogenicity of Earth's earliest fossils: A resolution of
1114 the controversy. *Gondwana Research* 22, 761-771.

1115 Sena, C.M., John, C.M., Jourdan, A., Vandesignste, V., Manning, C., 2014. Dolomitization of
1116 Lower Cretaceous Peritidal Carbonates By Modified Seawater: Constraints From Clumped
1117 Isotopic Paleothermometry, Elemental Chemistry, and Strontium Isotopes. *J. Sediment. Res.*
1118 84, 552-566.

1119 Sharp, Z., 2007. *Principles of Stable Isotope Geochemistry*. Pearson Prentice Hall, Upper Saddle
1120 River, NJ, 360 pp.

1121 Siedlecka, A., 1978. Late Precambrian Tidal-Flat Deposits and Algal Stromatolites in the
1122 Batsfjord Formation, East Finnmark, North Norway. *Sediment. Geol.* 21, 277-310.

1123 Sibley, D., 1978. Dolomite textures. In: Middleton, G.V., Church, M.J., Coniglio, M.,
1124 Hardie, L.A., Longstaffe, F.J. (Eds.), *Encyclopedia of Sediments and Sedimentary Rocks*.
1125 *Encyclopedia of Earth Sciences Series*. Springer, Dordrecht. pp. 231-234.

1126 Sibley, D.F., 1991. Secular changes in the amount and texture of dolomite. *Geology* 19, 151-
1127 154.

1128 Sibley, D.F., Gregg, J.M., 1987. Classification of Dolomite Rock Textures. *J. Sed. Petrol.* 57,
1129 967-975.

1130 Sijing, H., Keke, H., Jie, L., Yefang, L., 2014. The relationship between dolomite textures
1131 and their formation temperature: a case study from the Permian-Triassic of the Sichuan
1132 Basin and the Lower Paleozoic of the Tarim Basin. *Pet. Sci.* 11, 39-51.

1133 Stead, R.J., Kodama, K.P., 1984. Paleomagnetism of the Cambrian Rocks of the Great Valley of
1134 East Central Pennsylvania: Fold Test Constraints on the Age of Magnetization, Plate
1135 reconstruction. In: Van der Voo, R., Scotese, C.R., Bonhommet, N. (Eds.), *Paleozoic*
1136 *paleomagnetism: Interim report of the Working Group 2 on Phanerozoic Plate Motions and*
1137 *Orogenesis*. American Geophysical Union, Washington, D.C., pp. 120-130.

1138 Strauss, H., Beukes, N.J., 1996. Carbon and sulfur isotopic compositions of organic carbon and
1139 pyrite sediments from the Transvaal Supergroup, South Africa. *Precambr. Res.* 79, 57-71.

1140 Sugitani, K., Grey, K., Allwood, A., Nagaoka, T., Mimura, K., Minami, M., Marshall, C.P., Van
1141 Kranendonk, M.J., Walter, M.R., 2007. Diverse microstructures from Archaean chert from
1142 the Mount Goldsworthy–Mount Grant area, Pilbara Craton, Western Australia: Microfossils,
1143 dubiofossils, or pseudofossils? *Precambr. Res.* 158, 228-262.

1144 Summons, R.E., Amend, J.P., Bish, D., Buick, R., Cody, G.D., Des Marais, D.J., Dromart, G.,
1145 Eigenbrode J.L., Knoll, A.H., Sumner, D.Y., 2011. Preservation of Martian Organic and
1146 Environmental Records: Final Report of the Mars Biosignature Working Group.
1147 *Astrobiology* 11, 157-181.

1148 Swart, P.K., 2015. The geochemistry of carbonate diagenesis: The past, present, and future.
1149 *Sedimentology* 62, 1233-1304.

1150 Tilley, C., 1924. The Facies Classification of Metamorphic Rocks. *Geological Magazine* 61,
1151 167-170.

1152 Torgersen, T., Chivas, A.R., 1985. Terrestrial organic carbon in marine sediment: a preliminary
1153 balance for a mangrove environment derived from ^{13}C . *Chem. Geol.* 52, 379-390.

1154 Tucker, M., Wright, V.P., 1990. *Carbonate Sedimentology*. Blackwell Scientific Publications,
1155 Oxford, 482 pp.

1156 Vahrenkamp, V.C., Swart, P.K., 1990. New distribution coefficient for incorporation of
1157 strontium into dolomite and its implications for the formation of ancient dolomites. *Geology*
1158 18, 387-391.

1159 Van Kranendonk, M.J., Webb, G.E., Kamber, B.S., 2003. Geological and trace element evidence
1160 for a marine sedimentary environment of deposition and biogenicity of 3.45 Ga stromatolitic
1161 carbonates in the Pilbara Craton, and support for a reducing Archaean ocean. *Geobiology* 1,
1162 91-108.

1163 Van Zuilen, M.A., Fliegel, D., Wirth, R., Lepland, A., Qu, Y., Schreiber, A., Romashkin, A.E.,
1164 Philippot, P., 2012. Mineral-templated growth of natural graphite films. *Geochim.*
1165 *Cosmochim. Acta* 83, 252-262.

1166 Warren, J., 2000. Dolomite: occurrence, evolution, and economically important associations.
1167 *Earth-Sci. Rev.* 52, 1-81.

1168 Weller, S., 1903. The Paleozoic faunas. *New Jersey Geological Survey Report on Paleontology*,
1169 3, Trenton, NJ.

1170 Williford, K.H., Farley, K.A., Stack, K.M., Allwood, A.C., Beaty, D., Beegle, L.W., Bhartia, R.,
1171 Brown, A.J., de la Torre Juarez, M., Hamran, S-E., Hetch, M.H., Hurowitz, J.A., Rodriguez-
1172 Manfredi, J.A., Maurice, S., Milkovich, S., Wiens, R.C., 2018. The NASA Mars 2020 Rover
1173 Mission and the Search for Extraterrestrial Life. In: Cabrol, N.A., Grin, EA. (Eds.), *From*
1174 *Habitability to Life on Mars*. Amsterdam, Elsevier, pp. 275–308.

1175 Wilson, J.L., 1975. Carbonate Facies in Geologic History. Springer-Verlag, New York, 471 pp.

1176 Witte, R.W., Monteverde, D.H., 2012. Geologic History of New Jersey's Valley and Ridge

1177 Physiographic Province, New Jersey Geological and Water Survey Information Circular,

1178 Trenton, NJ.

1179 Wopenka, B., Pasteris, J.D., 1993. Structural characterization of kerogens to granulite-facies

1180 graphite: Applicability of Raman microprobe spectroscopy. Amer. Miner. 78, 533-557.

1181 Zhang, J., Hu, W., Qian, Y., Wang, X., Cao, J., Zhu, J., Li, Q., Xie, X., 2009. Formation of

1182 saddle dolomites in Upper Cambrian carbonates, western Tarim Basin (northwest China):

1183 Implications for fault-related fluid flow. Mar. Petrol. Geol. 26, 1428-1440.

1184

1185 **TABLES**1186 **Table 1.** Table of the samples analyzed using different methods.

Sample ID	Sample Description	Method				
		XRD	EPMA	CL	IRMS	Raman*
A18	dolarenite mudcracks	X				
A17	feldspathic dolarenite tidal channel deposit	X				
A16	dolosiltite domal stromatolite	X	X	X	X	X
A15a	chert lens	X			X	
B14	oolitic dolosiltite	X	X	X	X	
B13	oolitic dolosiltite	X			X	
B12a	oolitic dolarenite	X	X	X	X	X
B11	dolarenite	X	X	X	X	X
B10	oolitic dolarenite	X	X	X	X	
B9	oolitic dolosiltite	X			X	
A8	dolosiltite	X			X	
A7	oolitic dolosiltite	X	X	X	X	X
A6	feldspathic dolosiltite disk	X			X	
A5	oolitic dolosiltite thrombolite	X		X	X	X
A4	dolosiltite	X			X	
A3	dolosiltite with microstylolites	X	X	X	X	
A2	dolosiltite with solution seams	X			X	
A1	dolosiltite with solution seams			X	X	
B15b	dolomitic chert lens	X				
*12b	oolitic dolarenite	X				
*12c	oolitic dolarenite	X				
*12d	oolitic dolarenite	X				

x denotes sample analyzed

* denotes all samples analyzed by method but final representative samples used in paper are marked here

A,B,* denote sampling points marked on Fig. 3

1187

1188 **Table 2.** Stoichiometry and cation order within samples listed from bottommost to topmost

1189 sampled strata, *12d to A18, respectively.

Sample ID	Sample Description	Degree of Cation Order (d_{015}/d_{110})	Stoichiometry				
			d_{104} -spacing	XRD CaCO ₃ (mol%)	Mg/Ca	Microspar	EPMA (Mg/Ca)
A18	dolarenite mudcracks	0.654	2.890	51.23	0.95	-	-
A17	feldspathic dolarenite tidal channel deposit	0.604	2.888	50.69	0.97	-	-
A16	dolosiltite domal stromatolite	0.599	2.886	50.00	1.00	1.02	1.02
A15a	chert lens	n/a	n/a	n/a	n/a	-	-
B14	oolitic dolosiltite	0.659	2.893	52.33	0.91	1.02	n/a
B13	oolitic dolosiltite	0.619	2.893	52.33	0.91	-	-
B12a	oolitic dolarenite	0.848	2.893	52.33	0.91	1.03	1.04
B11	dolarenite	0.989	2.884	49.33	1.03	1.03	n/a
B10	oolitic dolarenite	0.640	2.893	52.33	0.91	1.03	n/a
B9	oolitic dolosiltite	0.491	2.893	52.33	0.91	-	-
A8	dolosiltite	0.375	2.893	52.33	0.91	-	-
A7	oolitic dolosiltite	0.900	2.893	52.33	0.91	1.02	1.03
A6	feldspathic dolosiltite disk	n/a	2.888	50.67	0.97	-	-
A5	oolitic dolosiltite thrombolite	0.596	2.885	49.67	1.01	-	-
A4	dolosiltite	0.737	2.894	52.67	0.90	-	-
A3	dolosiltite with microstyolites	0.683	2.893	52.33	0.91	1.02	1.04
A2	dolosiltite with solution seams	0.363	2.894	52.67	0.90	-	-
A1	dolosiltite with solution seams	-	-	-	-	-	-
B15b	dolomitic chert lens	n/a	2.854	39.33	1.54	-	-
*12b	oolitic dolarenite	0.656	2.889	51.10	0.96	-	-
*12c	oolitic dolarenite	0.772	2.891	51.61	0.94	-	-
*12d	oolitic dolarenite	0.788	2.890	51.35	0.95	-	-

dolosiltite = silt sized grains (5 μm - 63 μm)

n/a denotes no data from analysis

A,B,* denote sampling points marked on Fig. 3

dolarenite = sand sized grains (63 μm - 2 mm)

- denotes the sample was not analyzed

1190

1191 **Table 3.** Average D and G band values (pre-deconvolution of peaks) from microspar dolomite
 1192 phase within samples A16, A5, A7, B11, and B12a obtained from the cluster and Gaussian fit
 1193 methods showing overall comparable values among both peak processing methods used.

Cluster					
	I_D/I_G	G-FWHM	G position	D-FWHM	D position
Average	1.00	45.01	1600.54	68.42	1334.28
SD	0.01	3.48	5.29	13.91	4.11
Relative SD	1.40	7.74	0.33	20.33	0.31
Min	0.96	36.43	1594.66	49.06	1327.14
Max	1.02	50.33	1609.00	83.02	1339.00
Range	0.05	13.90	14.34	33.96	11.86
Gaussian fit					
	I_D/I_G	G-FWHM	G position	D-FWHM	D position
Average	1.02	44.21	1599.34	47.29	1335.40
SD	0.18	7.91	5.69	16.54	7.92
Relative SD	17.59	17.90	0.36	34.98	0.59
Min	0.70	25.17	1591.26	19.38	1321.59
Max	1.45	52.83	1608.52	75.88	1347.17
Range	0.75	27.66	17.26	56.50	25.58

1194

1195 **Table 4.** Derived temperatures (post-deconvolution of peaks) showing temperature variations as
1196 they appear in Fig. 12.

Sample ID	Sample Type	Temperature ($\pm 30^{\circ}\text{C}$)		T($^{\circ}\text{C}$) Range^a
		Fitting F*	Fitting E*	
A16	Stromatolite	314.53	315.37	301 $^{\circ}\text{C}$ - 319 $^{\circ}\text{C}$ (313 $^{\circ}\text{C}$ avg.)
		300.63	314.89	
		316.04	318.57	
B12a	Oolitic Dolarenite	296.62	316.55	297 $^{\circ}\text{C}$ - 322 $^{\circ}\text{C}$ (314 $^{\circ}\text{C}$ avg.)
B11	Dolarenite	314.81	321.59	
A7	Oolitic Dolosiltite	314.39	318.62	
A5	Thrombolite	260.33	274.34	260 $^{\circ}\text{C}$ - 287 $^{\circ}\text{C}$ (271 $^{\circ}\text{C}$ avg.)
		277.67	282.31	
		286.77	279.21	
		266.34	268.76	
		261.96	272.59	
		260.67	267.04	

^aTemperature range and average are taken from both fitting results

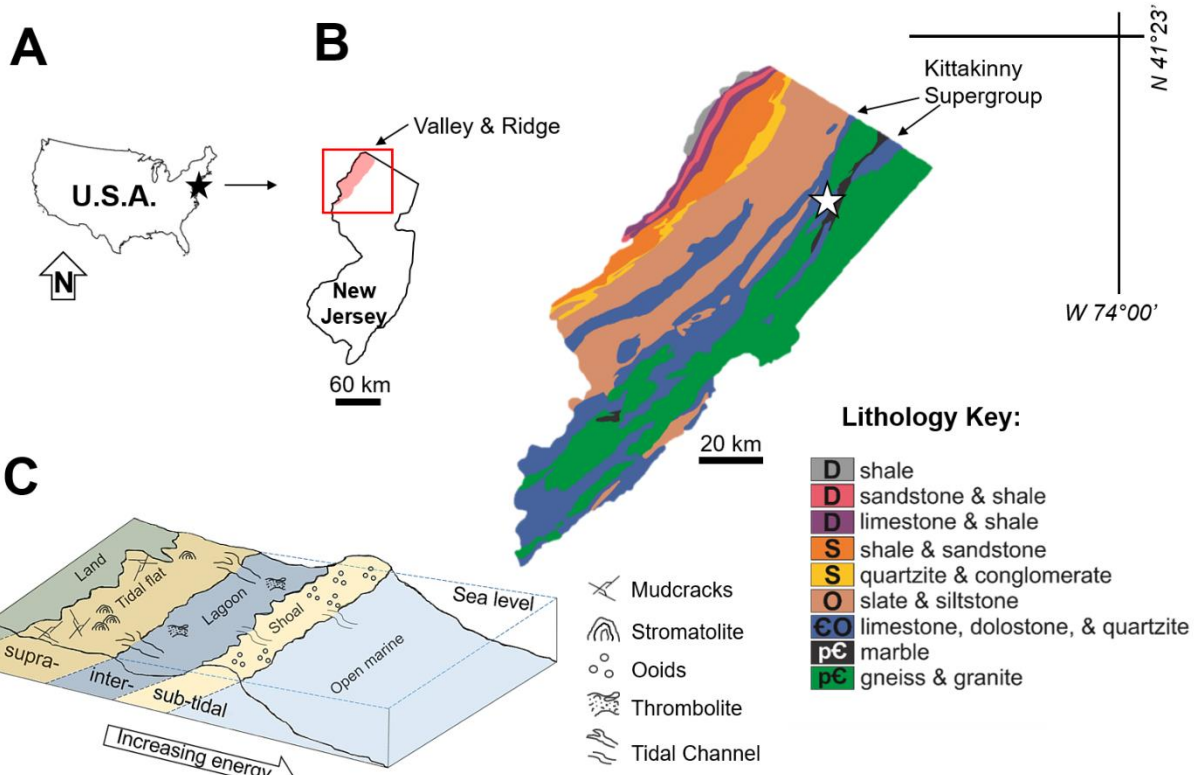
*Fitting procedures outlined in Kouketsu et al. (2014)

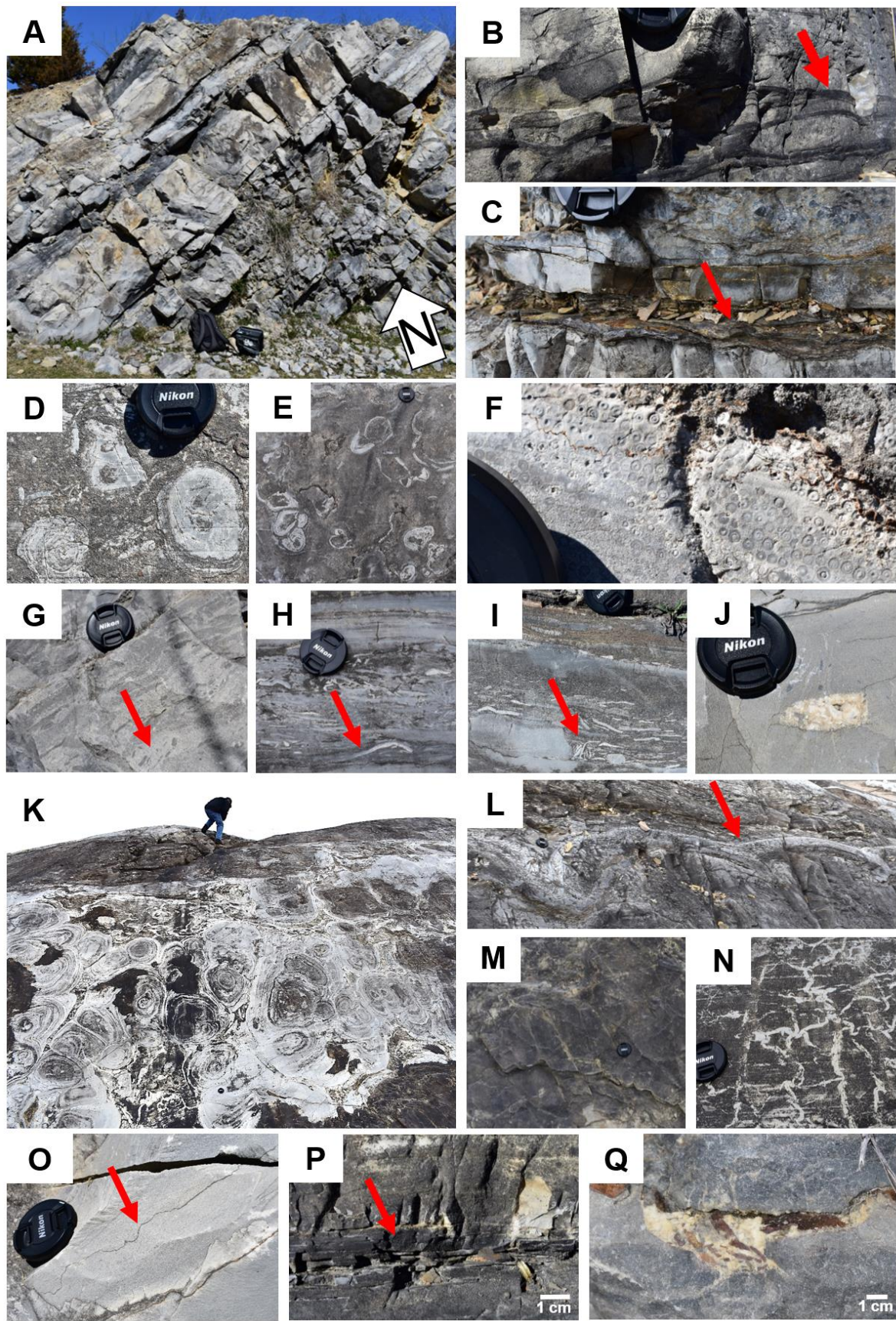
1197

1198

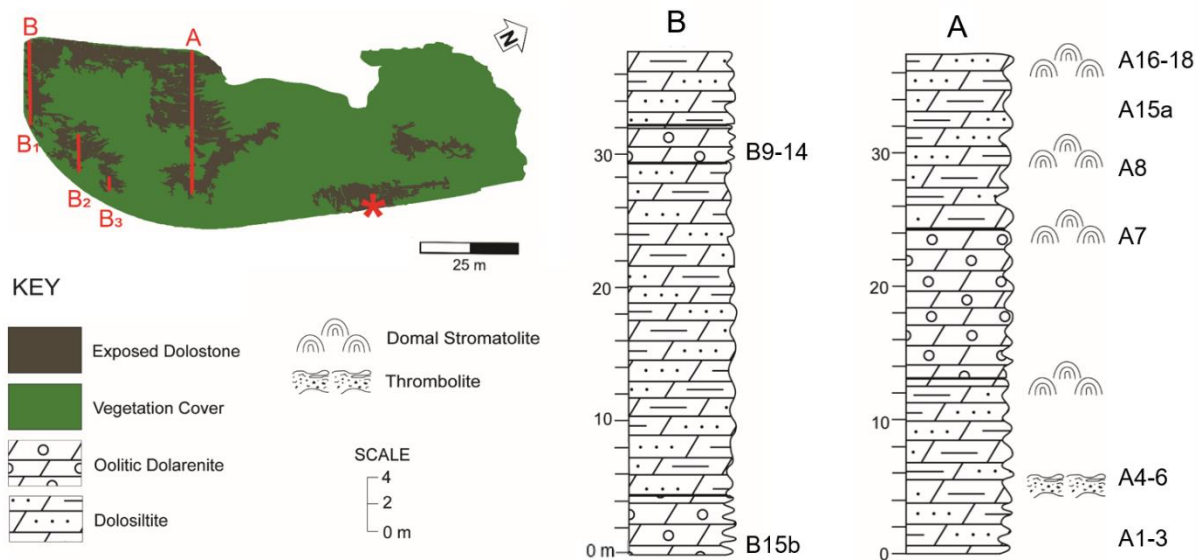
1199

1200 **FIGURES**



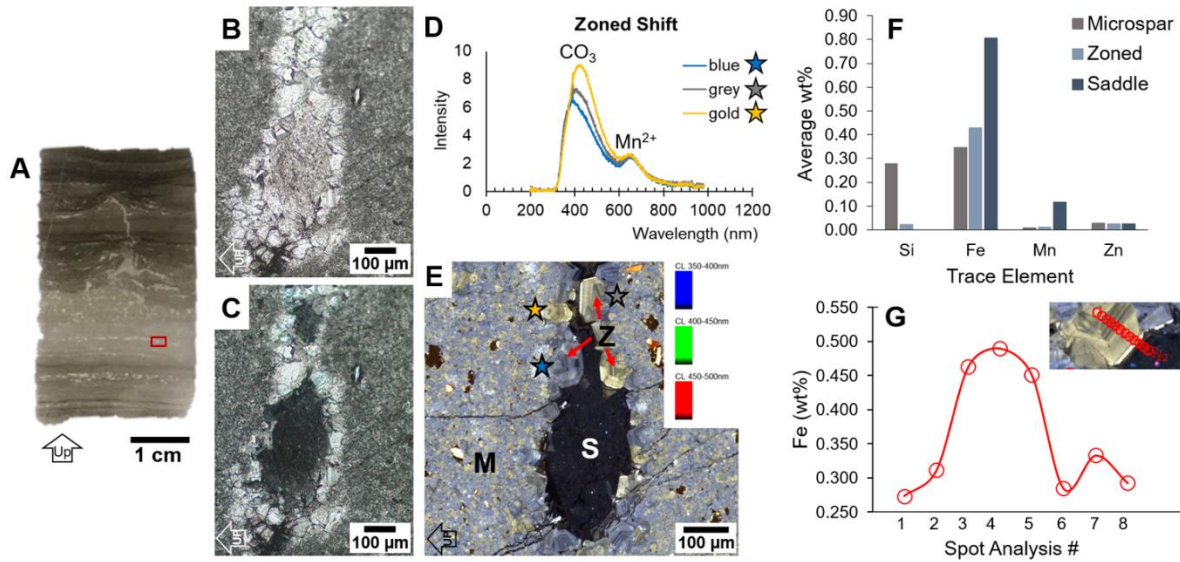


1210 **Fig. 2.** (A) Side view of Allentown Formation with tilted layers dipping 44° NW. (B) Dolosiltite
 1211 intercalated with solution seams. (C) Brown crinkled layer (red arrow) marks the top of
 1212 thrombolites (D) Small stromatolite heads. (E) Ripped up stromatolite heads. (F) Ooid
 1213 grainstone. (G) Dark grey rip-up clasts. (H) Edgewise conglomerates. (I) randomly dispersed
 1214 intraclasts. (J) Large vug filled with coarse-grained dolomite. (K) Top of formation with
 1215 glacially smoothed domal stromatolites (L) convex upward shape of stromatolites from NE side
 1216 of outcrop. (M) Mudcracks and (N) syneresis cracks visible from top of formation. (O) Wavy
 1217 stylolite parallel to bedding. (P) Black chert lens. (Q) Collapsed stylolite material into coarse-
 1218 grained dolomite filled vug. Nikon camera lens (5.5 cm radius) used for scale. All images are
 1219 cross sectional views except for D, E, K, M, and N which are planar views.



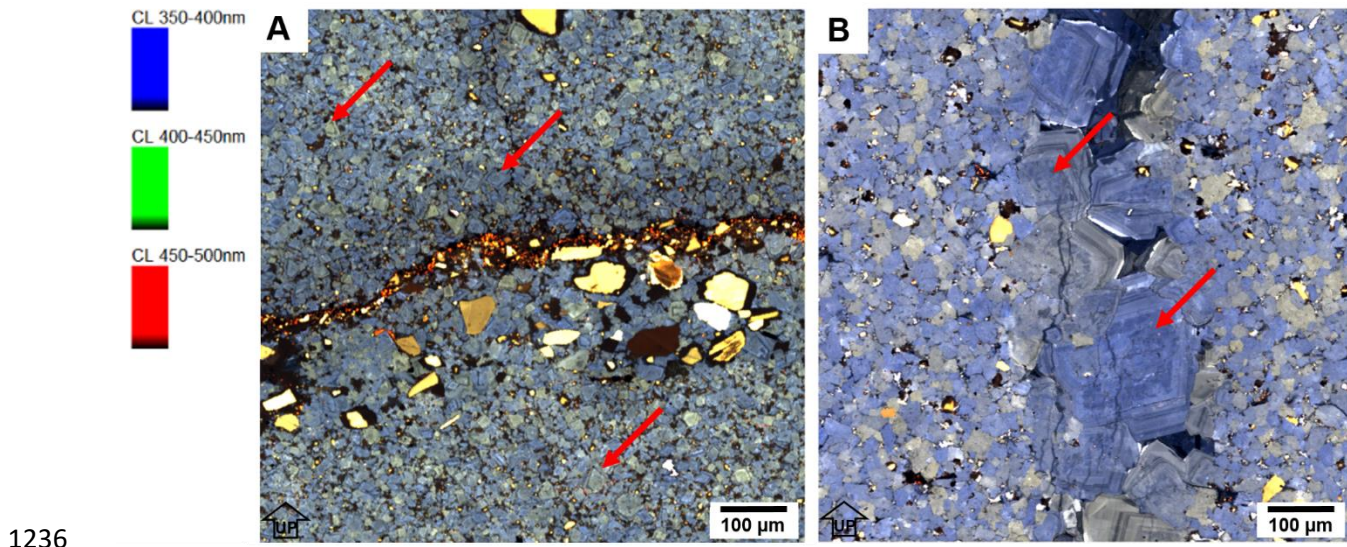
1220
 1221 **Fig. 3.** Stratigraphic columns made from sampled transects. Column B is exact bedding thickness
 1222 measured along B1, B2 and B3 (marked red on outcrop figure). Column A is estimated thickness
 1223 along glacially smoothed bedding measured along A (marked red). Asterisk (*) marks the
 1224 location of samples 12b-d (Table 2). Outcrop figure modified from aerial Google Earth imagery.

1225 Sampling points are marked by sample number to the right or each column to show where each
1226 sample type was collected.

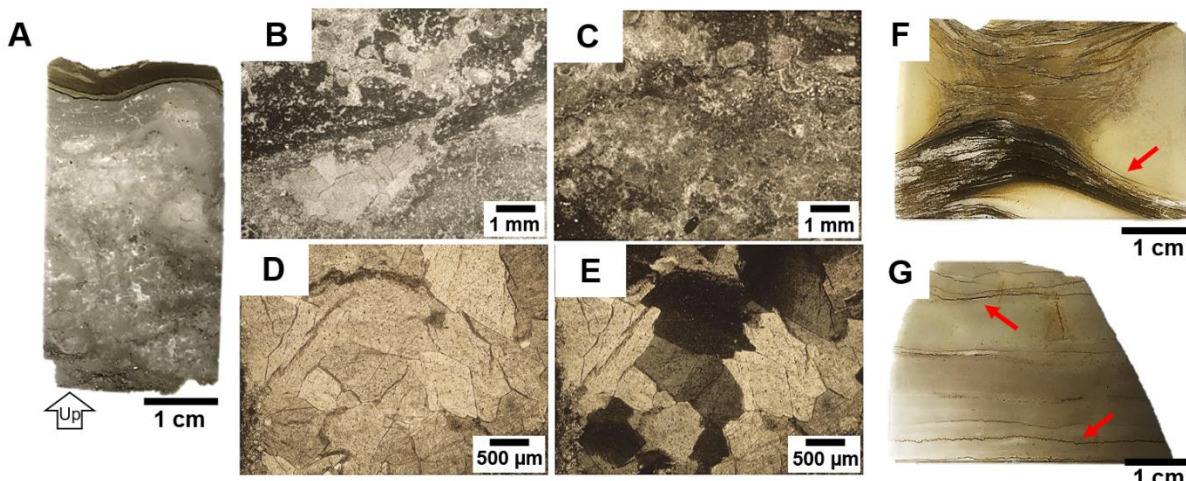


1227

1228 **Fig. 4.** CL and EPMA results. (A) Thin section of domal stromatolite (A16). Red box indicates
1229 mapped area in (E). (B) PPL photomicrograph of fenestral pore from sample (A). (C) Cross
1230 polarized light (XPL) photomicrograph of (B). (D) Characteristic spectra of luminescence colors
1231 showing a peak shift at CO_3 . (E) CL map showing three phases of dolomite: microspar (M),
1232 zoned (Z), and saddle (S) within sample (A). (F) EPMA spot analyses across each phase of
1233 dolomite within sample (A) showing the dolomitizing fluid compositional changes. (G) EPMA
1234 spot analysis across zoned dolomite within sample (A) reveals dark zonation bands are Fe-
1235 enriched.

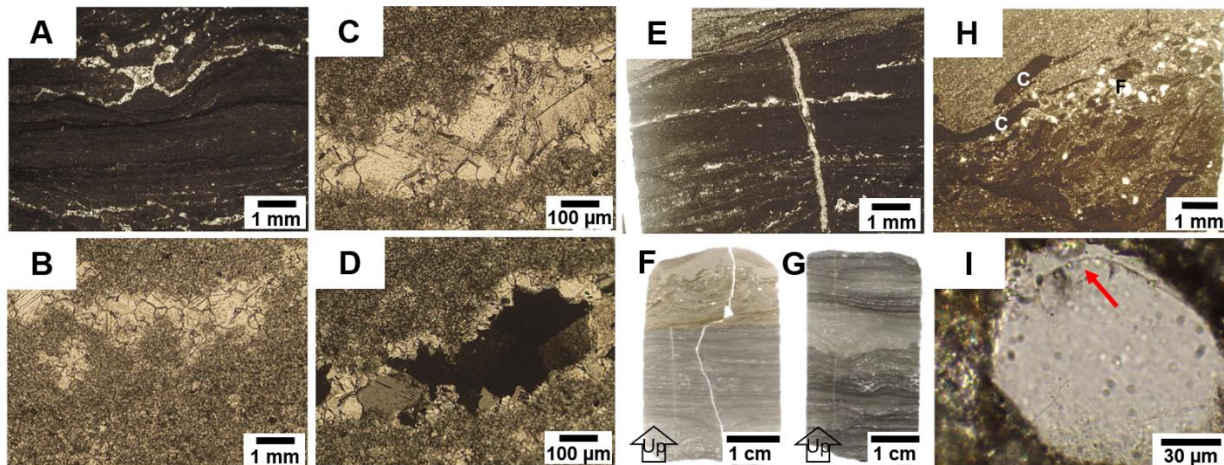


1236
 1237 **Fig. 5.** (A) CL map of microstylolite from dolosiltite sample A3 showing zoned rhombohedral
 1238 dolomite in pores of the microspar dolomite matrix (red arrows). Numerous feldspars (larger
 1239 yellow-brown grains) can be seen near the solution seam. (B) CL map of vertical microfracture
 1240 in dolarenite sample B11 showing zoned dolomite that lines and fills the microfracture. The
 1241 rhombohedral dolomite cores appear patchy in CL (red arrows).

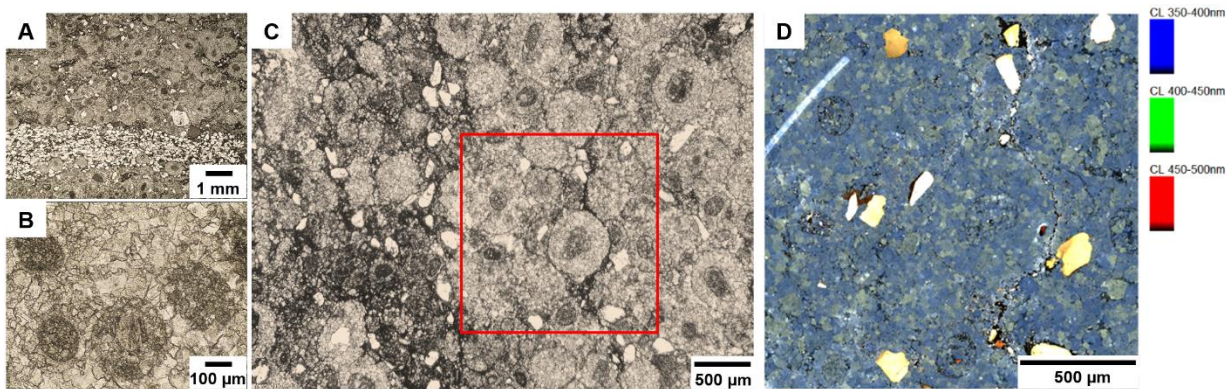


1242
 1243 **Fig. 6.** Subtidal lagoonal facies microtextures. (A) Thin section of thrombolite sample. PPL
 1244 photomicrographs of: (B) clotted structure and large saddle dolomite-filled vug, (C), clotted
 1245 thrombolite structure, and (D) large saddle dolomite filled vug indicative of burial

1246 dolomitization. (E) XPL photomicrograph of (D) shows sweeping extinction characteristic of
1247 saddle dolomite. (F) Thin section of dolosiltite sample (A1) with wispy solution seams (red
1248 arrow). (G) Thin section of dolosiltite sample (A3) with microstylolites (red arrows).

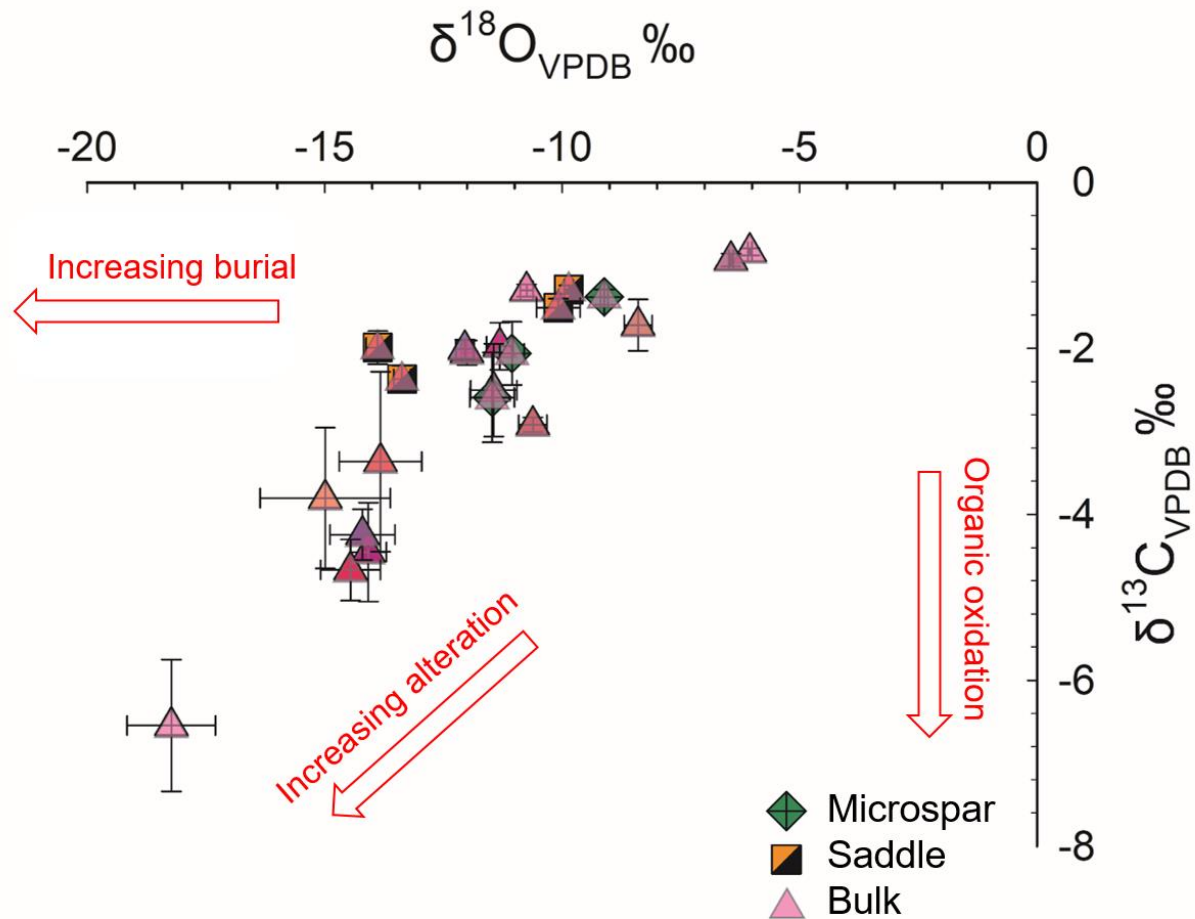


1249
1250 **Fig. 7.** Tidal flat stromatolitic facies microtextures. (A) Very fine laminae of finely crystalline
1251 dolomite, common in tidal flat stromatolites. Fenestrae (light colored areas in image) is filled
1252 with zoned and saddle dolomite; (B) Microspar dolomite and coarser-grained zoned dolomite-
1253 filled fenestrae; (C) Zoned and saddle dolomite-filled fenestrae surrounded by microspar; (D)
1254 XPL photomicrograph of (C); (E) preservation of primary fenestral porosity that is crosscut by
1255 secondary microfracture porosity, evidence for early, near-surface dolomitization; Thin sections
1256 of the top (F) and bottom (G) of a large domal stromatolite sample with corresponding PPL
1257 photomicrographs: (H) rip-up clasts (marked C) and feldspars (marked F) within topmost portion
1258 of dome (in F) indicate a tidal channel deposit; (I) Confocal Raman micrograph from (H) of an
1259 orthoclase overgrowth rim (red arrow).



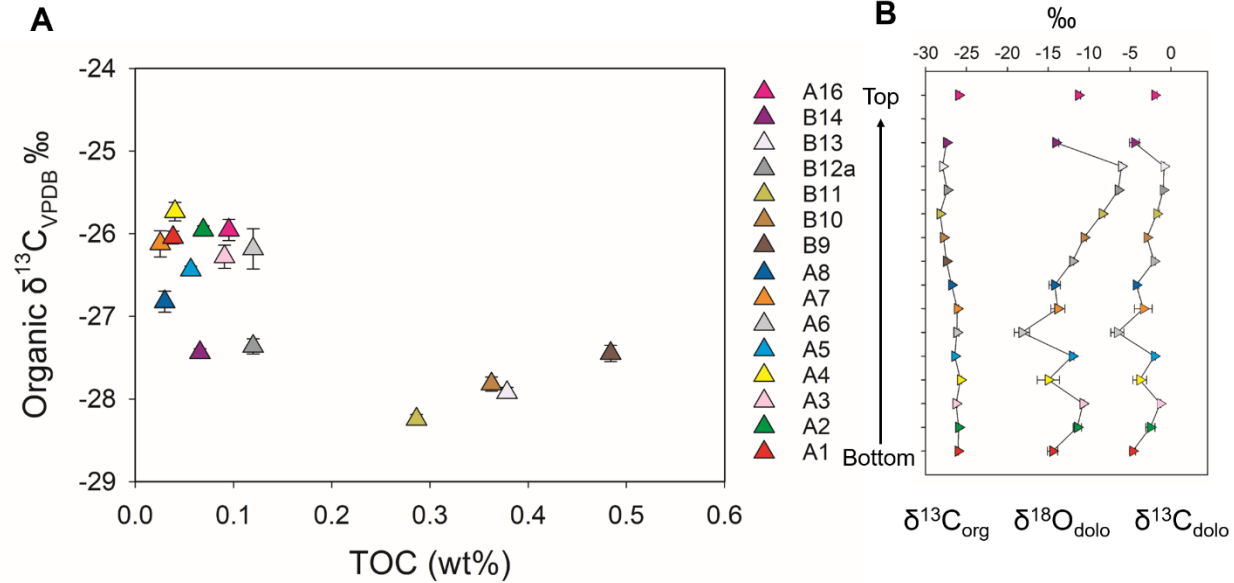
1260

1261 **Fig. 8.** Oolitic grainstone microtextures observed in thin sections. (A) PPL photomicrograph of
 1262 ooids (sample B10) with a finer-grained siliceous layer near the bottom of the image (white
 1263 area). (B) Photomicrograph in ppl of ooids from (A) showing dolomite replacement. (C) PPL
 1264 photomicrograph of CL mapped area (red box) in (D). (D) CL map showing characteristic violet
 1265 luminescence. Bright white and yellow grains are feldspars.



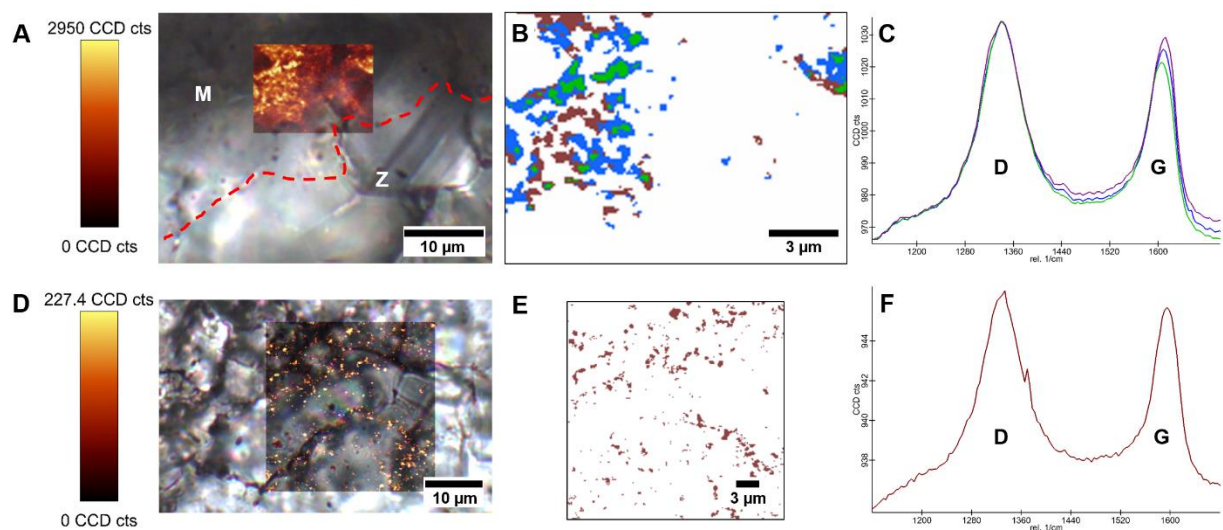
1266

1267 **Fig. 9.** $\delta^{13}\text{C}_{\text{dolo}}$ and $\delta^{18}\text{O}_{\text{dolo}}$ compositions measured from bulk samples, and micro-drilled
 1268 microspar and saddle dolomites. Overall alteration trends are marked by red arrows. Modified
 1269 from Allan and Wiggins (1993).



1270

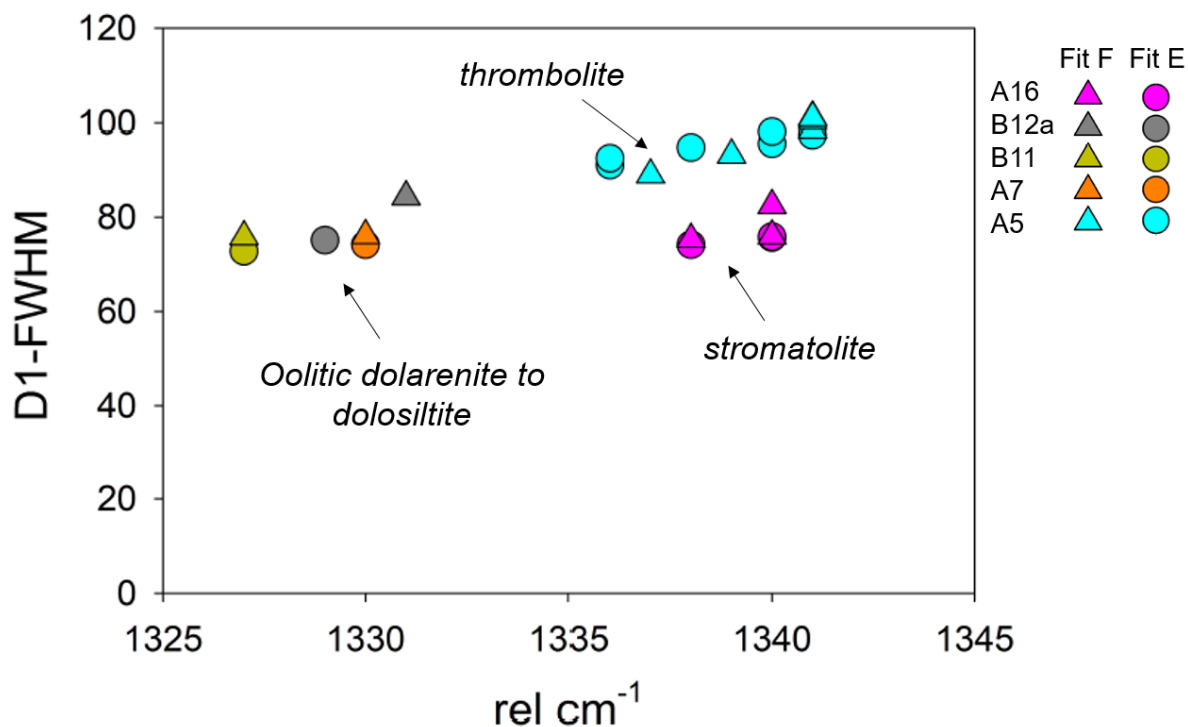
1271 **Fig. 10.** Graphs showing $\delta^{13}\text{C}_{\text{org}}$, $\delta^{18}\text{O}_{\text{dolo}}$, and $\delta^{13}\text{C}_{\text{dolo}}$ isotopic trends and TOC in Allentown
1272 dolostone. (A) Bi-plot of TOC wt% and $\delta^{13}\text{C}_{\text{org}}$ ‰ values. (B) The $\delta^{13}\text{C}_{\text{org}}$, $\delta^{18}\text{O}_{\text{dolo}}$, and $\delta^{13}\text{C}_{\text{dolo}}$
1273 isotopic trends across the outcrop reveal coupled $\delta^{18}\text{O}_{\text{dolo}}$ and $\delta^{13}\text{C}_{\text{dolo}}$ values, but $\delta^{18}\text{O}_{\text{dolo}}$ and
1274 $\delta^{13}\text{C}_{\text{dolo}}$ are decoupled with $\delta^{13}\text{C}_{\text{org}}$ isotopes. TOC error bars are obscured by symbols and are
1275 listed in Table S1 in supplementary material.



1276

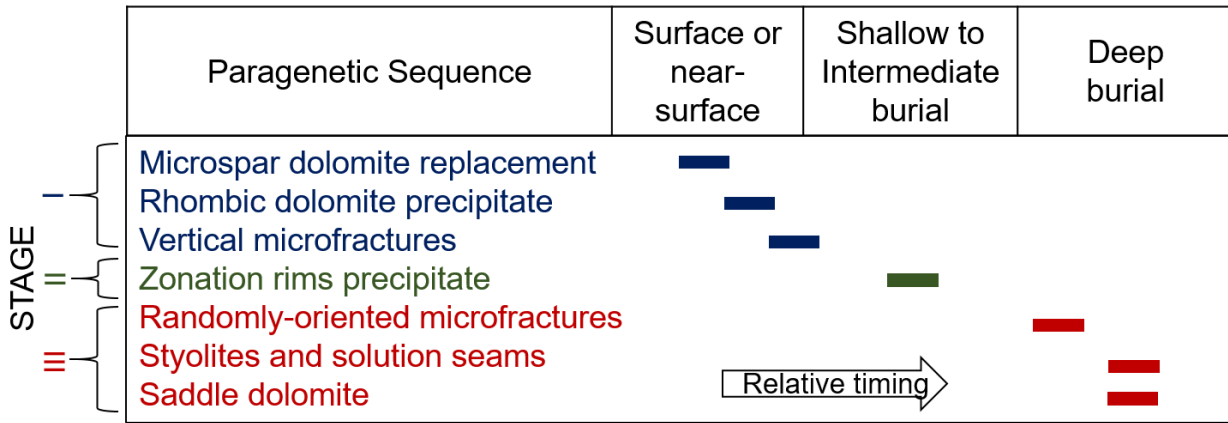
1277 **Fig. 11.** Raman cluster method example. (A) Transmitted light micrograph of stromatolite
1278 sample (A16) with overlay of Raman mapped D and G bands area. Bright yellow spots within

1279 the Raman map indicate spatial distribution of D and G bands before the cluster analysis. D and
 1280 G bands are associated only with the microspar phase of dolomite (marked M) but not the zoned
 1281 phase (marked Z). Note the z-depth (i.e., beneath sample surface) of confocal images reveals the
 1282 transition from M to Z, where M overlays Z near the boundary between phases. The boundary
 1283 determined from surface (z-depth=0) is marked with red dotted line. (B) Raman map after cluster
 1284 analyses of (A) showing differences in D and G bands averages and their spatial distribution. (C)
 1285 Overlay of D and G bands showing slight peak shift of G band which may indicate different
 1286 levels of crystallinity. (D) Transmitted light micrograph of oolitic sample (B12a) with overlay of
 1287 Raman mapped D and G bands area. Bright yellow spots within the Raman map indicate spatial
 1288 distribution of D and G bands within the microspar dolomite before the cluster analysis. (E)
 1289 Raman map after cluster analyses of (D) showing only one spectrum. (F). Raman spectra of D
 1290 and G bands which exhibits different peak parameters than the stromatolite sample in (C).



1291

1292 **Fig. 12.** Raman D1 band characteristics from cluster method after peak deconvolution, reveals
1293 that the samples group together by general facies type.



1294

1295 **Fig. 13.** Interpreted paragenetic sequence showing the formation of each dolomite phase with
1296 increasing burial depth. Modified from Hips et al. (2015).